# Infrared spectroscopy of live cells from a flowing solution using electrically-biased plasmonic metasurfaces†

Glen Kelp, [iD] [abc] Joy Li, [d] Junlan Lu, [iD] [b] Nicholas DiNapoli, [b] Robert Delgado, [iD] [b] Chao Liu, [e] Donglei Fan, [e] Shourya Dutta-Gupta [iD] [bf] and Gennady Shvets [iD] *[b]

Spectral cytopathology (SCP) is a promising label-free technique for diagnosing diseases and monitoring therapeutic outcomes using FTIR spectroscopy. In most cases, cells must be immobilized on a substrate prior to spectroscopic interrogation. This creates significant limitations for high throughput phenotypic whole-cell analysis, especially for the non-adherent cells. Here we demonstrate how metasurface-enhanced infrared reflection spectroscopy (MEIRS) can be applied to a continuous flow of live cell solution by applying AC voltage to metallic metasurfaces. By integrating metasurfaces with microfluidic delivery channels and attracting the cells to the metasurface *via* dielectrophoretic (DEP) force, we collect the infrared spectra of cells in real time within a minute, and correlate the spectra with simultaneously acquired images of the attracted cells. The resulting DEP-MEIRS technique paves the way for rapid SCP of complex cell-containing body fluids with low cell concentrations, and for the development of a wide range of label-free liquid biopsies.

## Introduction

Diagnostic differentiation of diseases based on studying individual cells, known as cytopathology, is commonly used in a clinical setting. Numerous diseases that can be identified and quantified on a cellular level, including certain cancers,[1,2] various infectious diseases,[3] and inflammatory conditions,[4] are successfully diagnosed by cytopathology. Compared to histopathology[5] (the study of tissues), another commonly used method, cytopathology is less invasive because it requires fewer cells that can be either exfoliated[6] or collected by fine needle aspiration.[7] Cytopathology relies on visual inspection of cells' morphology[8] after they have been stained using various contrast agents. Because this technique is inherently limited by fairly subjective interpretations of nuclear integrity, cellular size and structure, and stain uptake, the sensitivity of conventional cytopathology is often low.[9–11]

Alternatively, immunological methods rely on attaching tagged antibodies to specific over-expressed antigens on the cellular surface. Fluorescent molecules,[12,13] quantum dots,[14] and magnetic nanoparticles[15,16] have also been used as tagging agents. Unfortunately, the over-expression of target antigens, *e.g.*, epithelial cellular adhesion molecules (EpCAM) or prostate-specific antigen (PSA), is not always a reliable biomarker.[17] Nevertheless, immunological methods have found extensive clinical use, *e.g.*, for the enumeration of circulating tumor cells (CTCs) in blood samples.[18,19] Further sensitivity enhancement can also be obtained by combining immunological and morphological evaluations.[20,21]

On the other hand, a non-subjective and label-free method, such as infrared (IR) spectroscopy, is potentially very powerful because it probes intrinsic properties of cells: molecular vibrations of cells constituent molecules that are sensitive to the cell phenotype. Moreover, statistical chemometric techniques, such as multivariate analysis of the spectra,[22] enable removal of any subjectivity from the analysis in order to develop accurate fully-automated spectroscopic techniques of cell diagnosis referred spectral cytopathology (SCP).[23] Two inter-dependent challenges must be met in order to develop a clinically significant SCP procedure: (i) collecting the IR spectra from a small number of cells (monolayer or less, preferably in an aqueous environment) using a compact optical biosensor, and (ii) delivering and attaching the cells to an optical biosensor in the shortest possible time and with the least amount of cell

[a] *Department of Physics, University of Texas at Austin, Austin, Texas 78712, USA*
[b] *School of Applied and Engineering Physics, Cornell University, Ithaca, NY 14853, USA. E-mail: gshvets@cornell.edu*
[c] *Institute of Physics, University of Tartu, Tartu, 50411, Estonia*
[d] *Department of Biomedical Engineering, Cornell University, Ithaca, NY 14850, USA*
[e] *Department of Mechanical Engineering, University of Texas at Austin, Austin, Texas 78712, USA*
[f] *Department of Materials Science and Metallurgical Engineering, Indian Institute of Technology Hyderabad, Hyderabad, Telangana 502285, India*
† Electronic supplementary information (ESI) available. See DOI: 10.1039/c9lc01054h

modification. Below we present a short overview of various approaches to meeting these challenges that have been tried to date and describe our concept of simultaneous cell deposition and spectroscopic characterization of live cells in a flow that combines the concepts of dielectrophoresis (DEP) and metasurface-enhanced infrared reflection spectroscopy (MEIRS)[24] into an integrated device.

### Approaches to measuring cellular spectra

Several approaches to acquiring the IR spectra of live cells have been developed, as illustrated in Fig. S1.† These methods rely on transmission of IR light through a confluent monolayer of adherent cells[25–31] or use of attenuated total reflection (ATR) spectroscopy.[32–34] Of particular importance are the surface-enhanced techniques that have been employed in order to improve the sensitivity of spectroscopic measurements. Surface enhanced Raman spectroscopy (SERS) has been used for probing mid-IR vibrational modes of cells.[35,36] SERS has a number of limitations, such as long measurement times, need for sensitive detectors,[37–39] and possible photo-damage to cells from high intensity laser sources.[40] Surface-enhanced IR absorption spectroscopy (SEIRAS) is yet another method used to measure vibrational spectra of biomolecules by bringing them close to the sensor.[41–44] As we discuss below, there is an inherent challenge in applying surface-enhanced sensing techniques to non-adherent cells (e.g., lymphocytes or CTCs), and our work paves the way for addressing this underlying difficulty in applying SEIRAS to such biological systems.

A variant of SEIRAS is the metasurface-enhanced IR reflection spectroscopy (MEIRS, see Fig. 1a) utilized in this work and previously introduced by us to analyze fixed/dried cells.[24] Metasurfaces can be thought of as internal reflection elements (IREs) that localize evanescent fields in addition to providing local field enhancements characteristic of SEIRAS. Additionally, metasurfaces can be used to spectrally engineer mid-IR resonances, thus enabling high field enhancement and localization in the desired (fingerprint) spectral regions.[45,46] Mid-IR spectra obtained with the assistance of plasmonic metasurfaces[47] and antenna arrays[48,49] have been used for investigating protein monolayers, including the measurements of small proteins' spatial orientation[47] and real-time detection of secondary structure changes.[50] Further discussion of various methods used to obtain cellular spectra can be found in ESI.†

### Delivering cells onto optical biosensors

Even though surface-enhanced spectroscopic methods enable effective measurement of live cell spectra, depositing the cells onto the sensing surface presents an additional challenge, especially when high throughput measurements are desired or when non-adherent cells must be characterized. Cells can be drop-cast[51–54] onto either IR-transparent substrates or ATR prisms, followed by either drying, fixation, a combination of the two, or, ideally, retaining their natural aqueous environment. Microfluidic channels[51,55,56] have also been used to transport cells to optical biosensors. Most approaches rely on the gravity to push the cells to the surface of a biosensor at the bottom of the fluidic well. The subsequent immobilization of sedimented cells can be further expedited by functionalizing the sensor with antigen-specific antibodies.[57] However, gravity-based cell deposition can be rather slow, especially if the concentration of the cells suspended in solution is low.

Achieving full adherence on an IRE also requires considerable incubation time, typically multiple hours or even overnight.[58–60] Without full adherence to the IRE, the reflected spectra suffer from poor signal-to-noise ratio; external mechanical force application may be required to improve the spectra.[61,62] Ensuring close proximity of live cells to the IRE is even more challenging for non-adherent cells, such as normal and cancerous leukocytes and red blood cells.[60,63] Special chemical and structural modifications of the substrate are needed to keep such cells in good contact
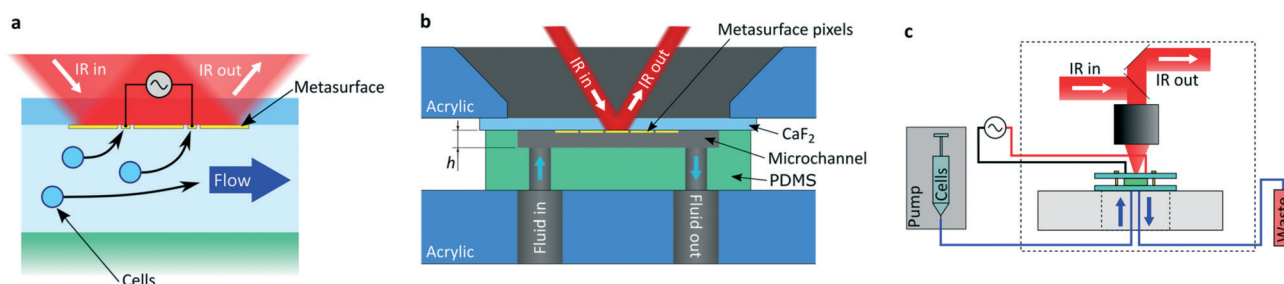


**Fig. 1** MEIRS sensor with integrated electrodes for DEP force generation. (a) Concept figure explaining how DEP–MEIRS sensor solves the problems of cell spectroscopy and delivery within an integrated device. The cells are pulled from the flow in microfluidic channel onto the metasurface by the DEP force generated by AC-biased wire electrodes, and spectra are collected using MEIRS. (b) Cross-section of the device (schematic). Cell solution is pumped through the microchannel (height $h$ = 64 μm) and cells are captured on the metasurface pixels by DEP force. IR reflection spectra from the metasurface are collected through the CaF$_2$ substrate. A window in the top acrylic clamp enables IR beam from the microscope objective to illuminate the metasurface and collect the reflected light. (c) Schematic of the experimental set-up. The sensor assembly shown in (b) is mounted on a microscope stage. Cells are injected into the microchannel using a syringe pump. AC voltage is applied to the wire electrodes embedded in the metasurface pixels.

**Paper**

**Lab on a Chip**

with the sensor,[64] including functionalization of the sensor with appropriate antibodies ("antibody chips").[60,65–68] Moreover, most commercially available IR microscopes, as well as most commercial SPR systems,[63] are upright, *i.e.* configured with optics on top of the fluidics. This further complicates the integration of the sedimentation-based cell deposition methods with existing commercial equipment.

Our approach to directing and capturing live cells onto a sensing metasurface uses the DEP attraction force. In the past, DEP has been used to separate and concentrate cells in solutions using various electrode configurations and microfluidic systems.[69–72] In related experiments, DEP forces have been used to boost the density of bacteria on SERS sensors[73,74] used for identifying human pathogens.

In this work we combine the ideas of DEP capturing and MEIRS-based characterization of live cells in an integrated microfluidic device (DEP-MEIRS) illustrated in Fig. 1a. The device utilizes a plasmonic metasurface to enhance the IR spectra of live cells obtained in reflection, combined with wire electrodes embedded in the metasurface to create non-uniform electric fields responsible for attractive DEP force. Combined with a microfluidics-based cells delivery system, we show that such a device can capture cells from a low-conductivity medium, and that their IR spectra can be simultaneously acquired.

Two human malignant cell lines (colorectal carcinoma HCT 116 and epidermoid carcinoma A431), as well as the polystyrene microspheres, are used in this study to demonstrate the capabilities and universality of the integrated DEP-MEIRS device. One of the key attractions of the DEP-MEIRS device is its scalability and wide dynamic range of cell solution volumes that can be spectroscopically interrogated. Specifically, in this work we analyze solution volumes of order 1 μL (about 1000 live cells) over the course of a 2 minute long measurement. However, by increasing the duration of the measurements and including a larger number of microfluidic channels, we could potentially analyze solution volumes that are 2 to 3 orders of magnitude larger. From a different perspective, much lower cell concentrations can be trapped and spectroscopically investigated. Thus, applications to clinically important tests such as the characterization of rare CTCs can potentially be enabled by the DEP-MEIRS approach.

## Results and discussion

### Description of the integrated DEP-MEIRS device

The concept of the DEP-MEIRS integrated microfluidic device is illustrated in Fig. 1. Details of the device fabrication and composition are provided in the Experimental section. Briefly, the device consists of two major components integrated into a single unit: the fluidic (delivery) part and the metasurface (sensing) part. The fluidic part is responsible for delivering live cells suspended in aqueous solution to the metasurface. The length of the channel (along the flow direction) is about 4 times longer than the length of the

sensing area, and it takes several seconds for a flowing cell to cross the entire sensor, during which time it must be captured by the DEP force and brought onto the metasurface. The sensing portion of the device consists of multiple plasmonic metasurfaces fabricated on an IR-transparent CaF$_2$ substrate, which is attached to the PDMS microchannel. An array of electrically-biased metallic wires is embedded into the sensor, each metasurface pixel having 2 embedded wires connected to the AC voltage source as shown in Fig. 1 and 2a. The resulting electric field between the wires attracts the cells to the metasurface-based optical sensor (Fig. 1a) *via* the DEP force. Once pressed onto the metasurface, the "squished" cells can be interrogated by MEIRS. The metasurfaces and the cells on them are illuminated by an IR beam through the IR-transparent CaF$_2$ substrate (Fig. 1b).

While well-known methods exist for permanently bonding glass (SiO$_2$) and PDMS for microfluidic use, in our case SiO$_2$ substrates cannot be used because they absorb mid-IR light. Therefore, the CaF$_2$ substrate is kept in tight water-proof contact with PDMS by mechanical clamping using custom made acrylic slides and bolted joints, thus providing a convenient way for mounting the sample into standard microscope slide holders.

Other ways to create microchannels on CaF$_2$ windows for IR transmission measurements have been proposed, using a thin layer (~20 μm) of either photoresist,[28–30] plastic[75] or paraffin[76] as the channel forming layer, or etching a microchannel straight into CaF$_2$.[77,78] For the former approach utilizing photoresist and plastic, two (top and bottom) CaF$_2$ windows could be sealed together by pressure and heating, and utilized for transmission measurements.

In our setup, there is no need for the entire stack to be IR transparent because the IR signal is collected in reflection mode. This enables us to utilize deeper micro-channels and to achieve higher flow rate $Q$ than would be possible in a transmission measurement. Water absorption is effectively cancelled by normalizing the reflection spectrum (acquired from the metasurface with cells on it) to the reference reflection spectrum (acquired from the metasurface in water, but without the cells).

### Metasurface-enhanced infrared reflection spectroscopy: with and without the cells

To illustrate the optical properties of the bare (cells-free) metasurfaces in reflection, two representative spectra (with and without water inside the microfluidic chamber) are shown in Fig. 2c for the metasurface pixel design used in this study. For the reflection spectra measured in air, two reflection peaks are observed. The maximum reflectivity feature on the high-wavenumber side of the spectrum corresponds to the dipole resonance of the metasurface, which is similar to the case of an array of plasmonic antennas.[48] The smaller reflectivity peak at a lower wavenumber arises due to Fano interference between the dipole and quadrupole resonances of the metasurface.[47] The
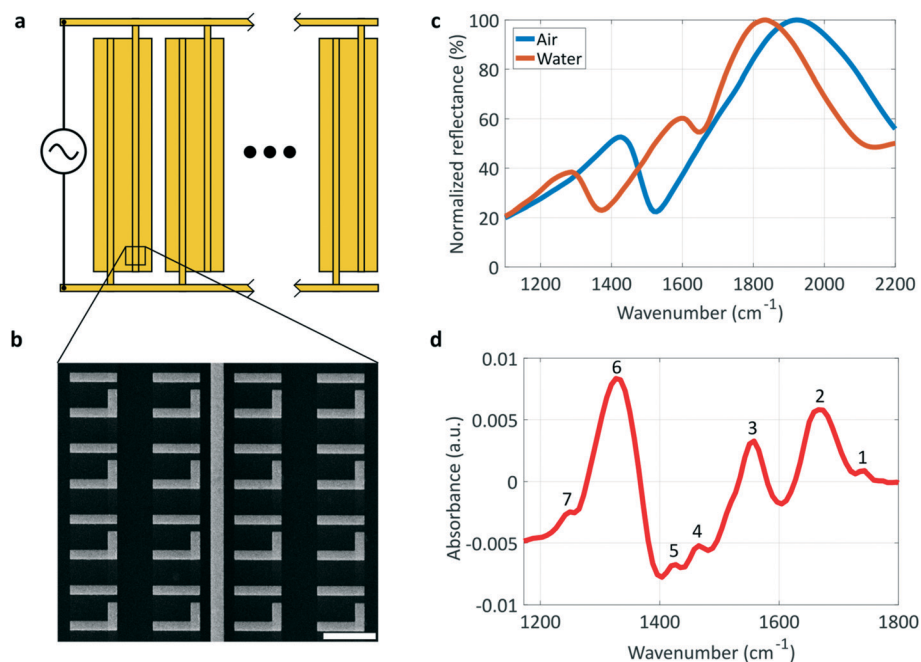
**Fig. 2** DEP-MEIRS sensor pixels with integrated electrodes and their IR spectra. (a) Schematic of the metasurface pixel array. (b) Enlarged SEM image of the metasurface pixel shown in (a). Scale bar is 2 μm. (c) Normalized reference reflection spectra of the metasurface pixel used in this work: in air (blue) and water (red). (d) Absorbance spectrum of the metasurface pixel with A431 cells on it.

same metasurface, when immersed in water, exhibits plasmonic resonances that are redshifted due to higher refractive index of the medium on top of the metasurface. A dip at 1650 cm$^{-1}$ is a characteristic feature caused by water absorption peak due to H–O–H bending.

The addition of biological cells greatly increases the complexity of the spectra because of the numerous identifiable vibrational resonances corresponding to the well-known vibrational modes of proteins, lipids, glycoproteins, and carbohydrates contained in the cell.[25] These features are not readily observable from the raw reflectance spectra of metasurfaces but become visible after absorbance spectra are calculated (see Experimental section). Metasurface spectra before and after cells' capture are used for calculating absorbance. A typical absorbance spectrum for A431 (human skin cancer) cells is shown on Fig. 2d. First it should be emphasized that, because the addition of the cells causes local refractive index to increase around the metasurface, the entire reflectance spectrum experiences a redshift. This puts the absorbance spectra on a non-flat baseline and creates a notable peak at the Fano resonance position ($\omega_F \approx 1330$ cm$^{-1}$ on Fig. 2d).

Nevertheless, the absorbance peaks of molecular vibrations due to cells can be clearly seen. The most significant peaks on Fig. 2d are the C=O stretching ($\omega_{C=O} \approx 1740$ cm$^{-1}$) in phospholipid esters, amide I ($\omega_{AmI} \approx 1660$ cm$^{-1}$) and amide II ($\omega_{AmII} \approx 1560$ cm$^{-1}$) protein vibrations, CH$_3$/CH$_2$ bending ($\omega_{CH} \approx 1460$ cm$^{-1}$) in lipids and proteins, –COO$^-$ symmetric stretching ($\omega_{COO} \approx 1420$ cm$^{-1}$), and a combination of asymmetric PO$_2$ stretching in phospholipids with amide III protein vibrations ($\omega_{PO_2, AmIII} \approx 1250$

cm$^{-1}$).[25,79–81] These vibrational modes and Fano peak are numbered on Fig. 2d from 1 to 7 and listed in Table 1. We note that the exact assignment of vibrational modes is rather challenging in the fingerprint region because many modes overlap there. Although a specific (fingerprint) spectral region is considered here, other molecular vibrations, such as C–O and PO$_2$ stretching modes of carbohydrates and phospholipids around 1000–1100 cm$^{-1}$, or CH$_3$/CH$_2$ stretching modes of the lipids around 2900 cm$^{-1}$ (ref. 25) can be targeted by rescaling the unit cell dimensions of the metasurface.

### Cell capturing by the DEP force

In this work, we concentrate on the high frequency regime of DEP for cell capturing, where the frequency of AC signal applied on the wire electrodes is above the crossover frequency of cells ($f \gg f_0$). Therefore, Clausius–Mossotti factor $K_{re}(f) > 0$ (see eqn (2) in Experimental section), and

**Table 1** Peaks observed in cell covered metasurface absorbance spectrum in Fig. 2d

| Peak | Wavenumber (cm$^{-1}$) | Vibrational mode assignment |
|------|------------------------|------------------------------|
| 1 | 1740 | C=O stretching |
| 2 | 1660 | Amide I |
| 3 | 1560 | Amide II |
| 4 | 1460 | CH$_3$/CH$_2$ bending |
| 5 | 1420 | –COO$^-$ symmetric stretching |
| 6 | 1330 | Fano resonance |
| 7 | 1250 | Asymmetric PO$_2$ stretching, amide III |

the cells behave as high field seekers, *i.e.* they are attracted to the regions of the highest electric field intensity $|\vec{E}_0|^2$. In the context of the microfluidic chamber shown in Fig. 1, this implies that the cells are attracted to the wire electrodes. Because the wires are embedded inside the metasurface, the cells are naturally attracted to the metasurface when AC voltage is applied to the wires. Thus, the attractive DEP force is used to press the cells upward against the sensor, enabling the acquisition of their vibrational spectra using the MEIRS technique as illustrated in Fig. 1. Although IR spectroscopy of living cells has been successfully utilized for a variety of applications, including distinguishing between cancerous and normal cells,[82] drug and malnutrition effects,[54,83] and FTIR imaging of sub-cellular structures,[84] to our knowledge this is the first demonstration of the integration of a plasmonic mid-IR optical sensor with a DEP electrode. The advantage of such integration is that the spectroscopic interrogation of live cells can be carried out in a matter of minutes, without any need for attaching the cells to the sensor. This is a particularly important consideration for non-adherent cells.

Note that according to eqn (2) and S1,† for lower frequencies the DEP force changes its sign and becomes negative for $f < f_0$. This property of the DEP force has been utilized for separating circulating tumor cells (CTCs) from the blood cells because the two cell types have different crossover frequencies.[70,85] However, cells separation is outside of the scope of this work.

The cell capturing capabilities of the DEP-MEIRS device were analyzed using numerical simulations (see Experimental section). A schematic of the microchannel geometry used in the simulations is shown on Fig. 3a.

Electric field (assumed to be electrostatic) generated in the flow channel over one electrode pair and the corresponding DEP force vector field are shown on Fig. 3c. Because $K_{re} > 0$, all the DEP force vectors across the channel are seen to point towards the wires in Fig. 3c. The force vector lengths are presented on a logarithmic scale because of very large amplitude variation of the DEP force across the channel. It is evident from the color plot of $|\vec{E}|^2$ on Fig. 3c that its gradient decreases with the distance from the electrode wires, and so does the DEP force. The maximum value of $|\vec{E}|^2$ is approximately $(10^6 \text{ V m}^{-1})^2$. DEP force magnitudes over a single electrode pair at different distances are represented on Fig. S6,† with comparison to gravity and flow induced forces.

Examples of particle trajectories in the simulated fluid flow and DEP force fields are shown on Fig. 3b. 40 particles evenly distributed in the *y*-direction at the inlet were used for visualization. Particle trajectories have been terminated at $\delta y_{min} = 5$ μm from the top and bottom surfaces, as this is approximately the lower limit of the radius for the cells and
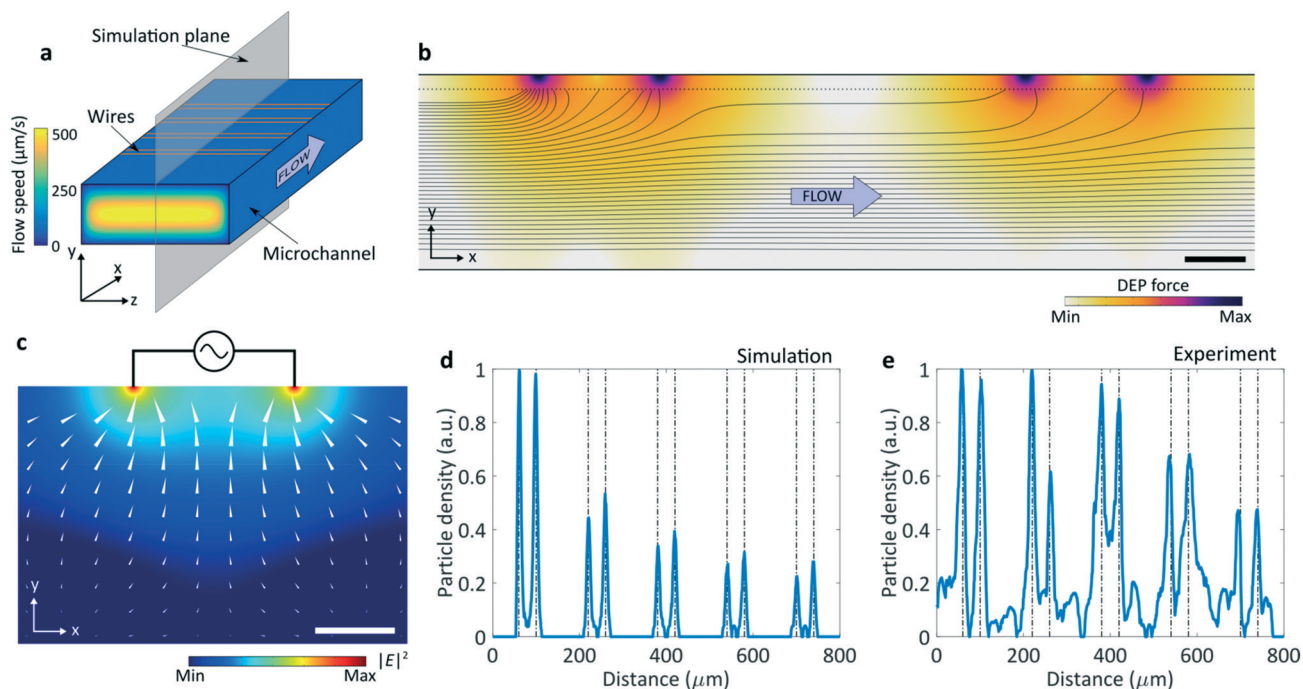


**Fig. 3** Numerical simulation of the particles capture in the microfluidic device. (a) Schematic of the microfluidic channel, with wire electrodes (4 pairs shown) on the top. Color-coded: fluid flow velocity. Fluid flow velocity at 5 μm distance (in *y*-direction) from the top surface of the channel is 127 μm s$^{-1}$ and at 10 μm distance 247 μm s$^{-1}$. (b) Example particle trajectories (dark blue lines, 40 all together) over the first two pixels (2 pairs of electrodes) in the 2D simulation plane defined in (a). Color plot: magnitude of the DEP force (in logarithmic scale). Scale bar: 20 μm. (c) Cut-out of the simulation domain showing single metasurface pixel (2 wires separated by 40 μm). White arrows: DEP force vectors (in logarithmic scale). Color plot: $|\vec{E}|^2$ (in logarithmic scale). Scale bar: 20 μm. (d) Simulated distribution of 10 μm diameter idealized particles and (e) measured distribution of 10 μm diameter polystyrene microspheres at matching $K_{re}$. Dashed lines on (d) and (e): locations of wire electrodes.

microspheres used in this study. The positive DEP effect is clearly seen from the particle trajectories shown in Fig. 3b: particles are pulled towards the electrodes, and as they get closer, the magnitude of the force increases while the fluid velocity decreases. If the particles are injected at a height close enough to the top surface, they eventually migrate to that surface and get captured. A much smaller proportion of the cells from the fluid layers located further away from the electrode surface are captured. This happens for two reasons.

First, the magnitude of the DEP force decreases and the required travel path length increases with the distance from the electrode. Second, the fluid velocity, and therefore the particle velocity, increases with the distance from the electrode. This decreases the time over which the DEP force is acting on the particles, thereby further reducing the probability of their capture. Based on these considerations, we conclude that those particles that are initially too far (in the $y$-direction) from the capturing electrodes flow through the entire length of the channel without reaching the top surface, or even drop to the bottom of the channel due to gravity and low fluid velocity. Note that for the overwhelming majority of the particles that are not too far from the electrode, the gravity (or, more precisely, anti-buoyancy) force is much smaller than the DEP force for the voltages used in this work[86,87] (see Fig. S6†).

An example of the final particle distribution from the simulation is plotted on Fig. 3d. The largest fraction of particles land on the wires, which agrees with the observations from Fig. 3b and c. Also, as seen from the particle trajectories on Fig. 3b, the upstream pixels (electrode pairs) capture more particles, and each adjacent pixel downstream captures fewer particles than the one before it. We also note that in a real continuous flow device, more particles pass through the cross-section of the channel per unit time at those points where the fluid velocity is higher. We have captured this effect in our simulation by making the density of the computational particles proportional to the flow velocity and injecting each of them only once. Altogether, $N_{macro}$ = 1000 computational particles were used to generate the data in Fig. 3d. Weighing the initial particle density values with flow velocity at the inlet mimics continuous stream of particles in a simulation where particles are. Examples of particle distributions for different
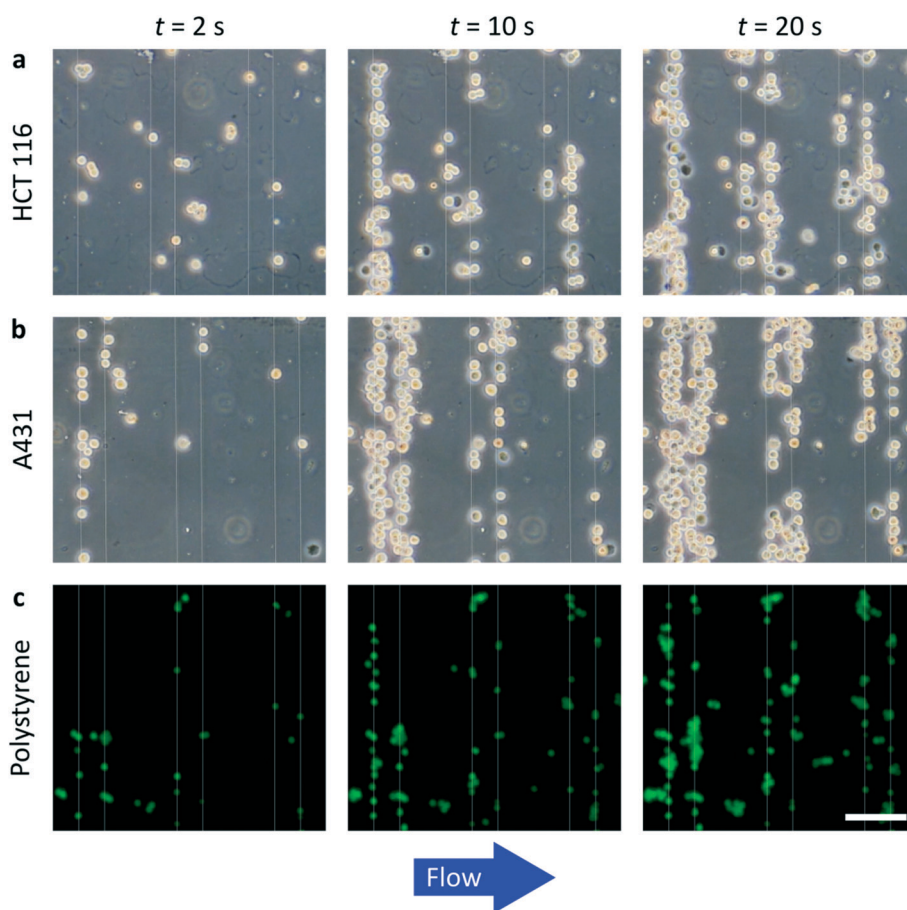


**Fig. 4** Capturing cells and solid microspheres from a flow onto wire electrodes using DEP force. (a) HCT 116 cells, (b) A431 cells, and (c) 10 μm diameter fluorescent polystyrene microspheres collected on wire electrodes by DEP force. Three different time instances are shown: 2 s, 10 s and 20 s after the start of the flow. Cells were imaged in the phase contrast mode. Fluorescent microspheres were illuminated with a 395 nm excitation light. Fluid flow direction: from left to right, flow rate: $Q$ = 0.01 μL s$^{-1}$. Positions of the wires are marked with vertical light colored lines. Scale bar: 100 μm for all images.

values of the voltage applied across the wires are shown in Fig. S7.† The results of experimental measurements of DEP capturing of live cells and polystyrene microspheres are presented below.

**Experimental demonstration of the DEP capture of cells and microspheres**

In order to demonstrate the DEP capture of microscopic objects from a flow through the proposed microfluidic device, a series of experiments was conducted with (i) HCT 116 and (ii) A431 immortalized cell lines (human colon and skin cancer, respectively), and (iii) 10 µm diameter polystyrene microspheres. The three types of microparticles collected onto the wire electrodes are shown in Fig. 4a–c. Even though our metasurfaces are sufficiently transmissive for visible light to enable visible light imaging of adequate quality, for the experiments below we used samples with wire electrodes (but no metasurfaces) in order to further enhance the imaging quality. This is justified by noting that metasurfaces act as field-enhancing IREs but play less significant role in modifying the DEP force due to their planar nature, while the electric fields responsible for particle capturing are distributed in full 3-dimensional configuration. The use of only wire electrodes is further justified by noting

the similarity of cell collection patters with and without metasurface elements (see Fig. 4a and b and 5c–e).

The operating frequency $f$ of the AC signal applied to DEP electrodes was selected while keeping in mind that the sign and magnitude of the DEP force at a given frequency depends on the cell type and on the properties of the solid particles.[88] The frequency dependence of the CM factor $K_{re}(f)$ appearing in eqn (2) was experimentally determined for all micro-particles used in this work by utilizing a standard hyperbolic electrode geometry.[89,90] The obtained CM factors are plotted in Fig. S3,† and the experimental technique is explained in the ESI† Methods ("Characterization of the frequency dependence of the DEP force for live cells").

Experimentally obtained crossover frequencies are $f_0^{(HCT)} = 111 \pm 24$ kHz for the HCT 116 cells and $f_0^{(A431)} = 86 \pm 20$ kHz for the A431 cells at DEP solution conductivity $\sigma_s = 781.3 \pm 1.1$ µS cm$^{-1}$ ($f_0$ is dependent on $\sigma_s$ value). Based on these findings, the AC signal frequency used in all cells experiments described below was $f^{(cell)} = 400$ kHz $\gg f_0^{(HCT)}$, $f_0^{(A431)}$ corresponding to $K_{re} \approx 0.7 - 0.9$ for both cell types. On the other hand, $f^{(ms)} = 200$ Hz was used to capture the 10 µm diameter fluorescent polystyrene microspheres. Fluorescent particles were chosen due to the ability to fully suppress image background (black area on Fig. 4c) for faster and more reliable data analysis.
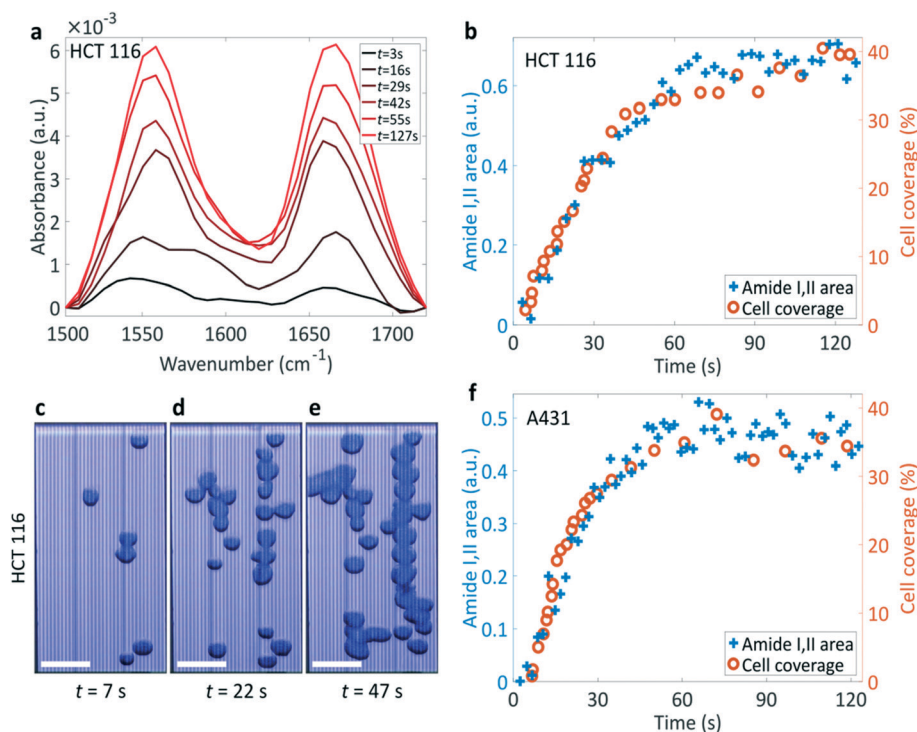


**Fig. 5** Combined action of DEP capturing and mid-infrared reflection spectroscopy (MEIRS) on flowing solutions of HCT 116 and A431 cells. (a) Baseline-corrected absorbance spectra of HCT 116 cells in the amide I and amide II band collected at different times. Emergence of the amide I, II peaks is observed as more cells attach onto the metasurface due to DEP attraction. (b) Area integrated under the amide I and II absorbance spectra (blue crosses) and the fractional cell coverage of the pixel (red open circles) for HCT 116 cells. (c)–(e) Images of the HCT 116 cells attracted onto the metasurface pixel at three different time points ($t_i$ = 7 s, 22 s and 47 s). The pixel area covered by the cells has been digitally enhanced for better visibility. Flow direction is from left to right. (f) Same as (b), but for A431 cells. Fluid flow rate: $Q$ = 0.01 µL s$^{-1}$. Scale bars in (c)–(e): 40 µm.

It can be observed from Fig. 4a–c that more cells and microspheres become trapped by the upstream electrodes (on the left) than by the downstream ones (on the right), as predicted by numerical simulations. The cells are observed to form lines at the wire locations (Fig. 4a and b). Even though most cells land directly on top of the wires, they tend to drift further downstream to a new equilibrium position, typically about one cell radius away from the wire. Most cells also appear to be attaching to the surface after the initial landing. Within tens of seconds, the cells drift to the equilibrium position, where they stay afterwards. It was experimentally verified that most of the attached cells can be removed from the sensor surface by turning off the AC signal, applying low-frequency electric field to the wires, resulting in a repelling (negative-DEP) force, or when the fluid flow rate $Q$ is significantly increased.

The polystyrene microspheres attracted to the wires for $f = f^{(ms)}$ exhibit distribution patterns that are similar to those of the cells, as can be seen in Fig. 4c. One important distinction between cells and microspheres is that the former experience positive DEP force at higher signal frequencies, while the latter experience positive DEP force at lower frequencies. The other important difference between the two is the nature of their attachment to the metasurface: the polystyrene particles stay at their landing spot and do not shift downstream by a couple of microns as the cells do.

For the microspheres, the experimentally measured particle distribution (Fig. 3e) is compared with the simulation results (Fig. 3d). As predicted from the simulations, the majority of the particles are indeed captured at the locations of the wires, and an overall trend of particle density reduction downstream is clearly observed. However, the density reduction is less pronounced in the experiments than in simulation. There are several reasons for this discrepancy.

First, our simulations do not take into account the possibility of particle release due to fluid flow after capturing. Second, particles that have already landed on the wires alter the electric fields generated around that wire. This effect is not captured by the simulation, causing fewer particles to be captured upstream. Third, simple steric effects can alter particles' distribution. For example, the already captured particles can prevent the incoming ones from being captured at the same location. As the upstream wires fill up with particles, more of the incoming particles get attracted to the wires downstream, causing their experimental distribution to be more even than numerical simulation predictions.

The same effects are present for the cells, although their exact manifestations differ. For example, we found that constant fluid flow itself can exert sufficient force to detach some of the cells from their original landing spots and carry them to next wire electrode downstream or even all the way to the exit port. Unlike microspheres, there is considerable heterogeneity in the sizes and membrane areas of the cells. Individual cells with smaller membrane areas would be easier to detach because the DEP force acting on them at a given frequency is smaller than the force acting on cells with larger membrane areas.[86]

Overall, we find that despite some differences, there are many commonalities between DEP trapping of cells and microspheres. This demonstrates the universality of the DEP trapping approach and suggests that other types of small particles could be captured onto, and spectroscopically interrogated by, a DEP-MEIRS microfluidic device described here. Next, we restrict our analysis to living cells and demonstrate the possibility of spectral interrogation of cells in a flow using DEP-MEIRS.

## Spectroscopy of cells collected from a flowing solution

The full capabilities of the integrated DEP-MEIRS device were demonstrated in the experiments where the IR spectra were collected over several minutes while the cells were pumped through the microchannel and captured onto the sensor surface using the DEP force. A schematic of the experimental set-up is shown on Fig. 1c; see Experimental section for the details of the DEP capture. Briefly, prior to the measurements, the cells were transferred to low-conductivity buffer (the "DEP solution")[70] and then injected into the chamber using the syringe pump. For the DEP capture of the cells, the AC voltage and frequency applied between the adjacent electrode wires were $V_{pp}$ = 14 V (peak-to-peak) and $f^{(cell)}$ = 400 kHz, respectively. Only one of the 12 metasurface pixels (4th one downstream) was used for spectral measurements.

While many vibrational lines are observed in the spectrum (see Fig. 2d and Table 1), in the rest of the paper we concentrate on the three most prominent spectral features: the Fano resonance ($\omega_F \approx 1330$ cm$^{-1}$), the amide I vibration ($\omega_{AmI} \approx 1660$ cm$^{-1}$), and the amide II vibration ($\omega_{AmII} \approx 1560$ cm$^{-1}$). Note that the frequencies of the two latter vibrational modes fall between those of the dipole ($\omega_D \approx 1830$ cm$^{-1}$) and the Fano resonances of the metasurface (Fig. 2c). This is precisely the spectral region where the evanescent field enhancement is high and nearly frequency-independent.[24] Therefore, the amide I, II vibrational modes are expected to be the spectral biomarkers that are particularly sensitive to the cells' attachment to the metasurface.

The absorbance spectra were calculated for every collected reflectance spectrum at different time instances, and the spectra were collected every $\Delta t$ = 3 s (see Experimental section). The reflectance spectrum at the beginning of the experiment, i.e. prior to the injection of cells into the microfluidic chamber, was used as a reference. The emerging amide I and II features in the baseline-corrected absorbance spectra collected as a function of time after the start of the flow of the HCT 116 cells solution is shown in Fig. 5a. The total area under the amide I and II features in the absorbance spectra correlates well with the total area of the metasurface covered with cells as shown in Fig. 5b.

The cell coverage was measured from the images of the cells that were recorded in transmission (i.e. using

illumination from below through the PDMS chamber) simultaneously with the spectra: see Fig. 5c–e for the images of HCT 116 cells on top of the metasurface at three different times. The capability of simultaneously collecting the visual images of the cells and their infrared spectra is one of the attractive features of MEIRS based SCP because plasmonic metasurfaces provide considerable transparency for visible light combined with significant reflectivity for the mid-IR radiation. The strong correlation between the cell coverage (red circles in Fig. 5b and f for HCT 116 and A431 cell solutions, respectively) and the amide I, II absorptivity (blue crosses in the same figures) clearly indicate that the observed spectral features indeed originate from the cells' attraction to the metasurface.

In addition to vibrational resonances of the cells, the plasmonic resonance of the metasurface at the Fano resonance frequency $\omega_F$ also manifests itself as an absorption peak as the cells are collected on the metasurface (see Fig. 2d and Table 1, peak number 6). This feature is not associated with any native vibrational modes of the cell. Instead, it emerges as the metasurface reflection spectrum undergoes a redshift due to higher refractive index of the cells compared with that of water. In the absorbance spectrum this spectral redshift translates into a peak (see Fig. S8† and 2d).

Owing to its high quality factor ($\sim$10), this plasmonic resonance is very sensitive to local refractive index changes in the immediate vicinity of the metasurface. Because the characteristic field penetration length for this metasurface design is $l_{pen} \sim 100$ nm,[24] the peak in the absorbance spectrum at the Fano feature is proportional to the area of the metasurface which is in intimate contact (closer than $l_{pen}$) with the cells. We expect that this area is proportional (although inevitably smaller) than the cell coverage area. Therefore, the magnitude of the Fano feature can be used as a proxy for cell coverage in those cases when the combined image and spectral acquisition is not possible. This hypothesis is confirmed by the experimental data shown in Fig. 6, where the cell coverage (red open circles in Fig. 6b and c) is clearly correlated with area under the baseline-corrected Fano feature in absorbance spectrum (blue crosses).

Because the magnitude of the Fano absorbance feature is sensitive only to the local refractive index change at the resonant frequency $\omega = \omega_F$ and not to any specific molecular fingerprints, it cannot be effectively used to distinguish between cell types. Nevertheless, our data indicates that the magnitude of Fano absorbance can be used as a measure of cell coverage in those cases when sub-monolayers of cells are considered. This could be particularly useful when visual images of the attracted cells, such as the ones presented in Fig. 5c–e, cannot be easily collected. Therefore, one potential advantage offered by MEIRS is in combining the information obtained from the high-$Q$ Fano resonance (e.g., the estimate of the number of cells on the sensor) with the cell-specific vibrational information from the rest of the high-reflectivity spectral range. However, spectroscopic distinguishing between cell types is outside of the scope of this work.

### Relationships between changes in vibrational spectra and cells' attraction to metasurfaces

To ensure that the observed time-dependent vibrational spectra shown in Fig. 5a are indeed related to the DEP attraction of cells from the DEP medium to metasurfaces, we investigated other potential sources of spectral variation. One contributor to the increasing amide I,II and Fano features observed in Fig. 5b and f and 6b and c that are not directly caused by the growing number of cells on the metasurface are caused by small molecules' DEP trapping.[91–93] Such trapping could cause slight increases in the amide and Fano signals due to the presence of the residual proteins in the solution. The presence of proteins in solution could be due to residual cell debris and culture media. That even a single layer of proteins can be easily detected using very similar metasurfaces has been demonstrated in our earlier work.[47]

Therefore, a control measurement (see Experimental section) that involves flowing a cell-free protein solution through the DEP-MEIRS microfluidic device was carried out to establish upper bounds on the amide I, II and Fano absorbance not related to the attraction of the cells. The obtained time-varying absorbance spectra were used to
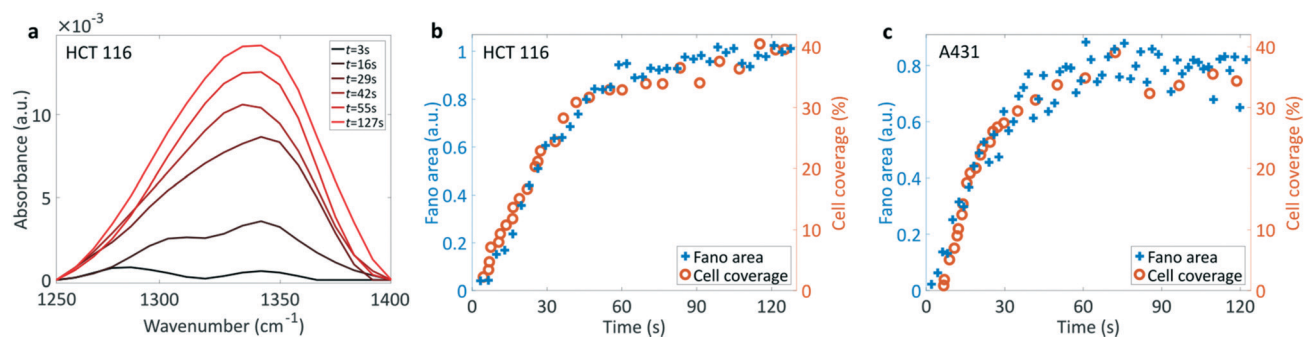


**Fig. 6** Cell coverage correlates with the Fano feature. (a) Emergence of the metasurface Fano resonance feature in the absorbance spectrum (baseline corrected) of HCT 116 cells. As the cell coverage increases, so does the height of the peak associated with Fano feature. (b) Area calculated under the Fano feature in (a) (blue crosses) superimposed on the fractional cell coverage (open red circles) of the pixel for HCT 116 cells. (c) Same as (b) but for A431 cells.

calculate the baseline (see Fig. S9†) that was subtracted from the absorbance data to obtain Fig. 5b and f and 6b and c (blue crosses). The medium concentration was chosen so as to match the finite slope of the time-varying absorbance spectra that needs to be removed as part of the baseline correction procedure. The background signal was subtracted from the raw data because its accumulation rate is constant throughout the experiment. As we observe by comparing Fig. 5 and 6 to Fig. S9,† the residual contribution of trapped proteins to the spectra is almost an order of magnitude smaller than the contribution from the cells over the same time period. Therefore, this baseline measurement demonstrates that the spectral modifications shown in Fig. 5 and 6 primarily originate from the attracted cells. This validates the excellent correlation between the strength of the spectral features and the areal coverage of the sensor by captured cells.

## Conclusions

In this article we have described a new approach to collecting vibrational (mid-IR) spectra of live cells: dielectrophoretic (DEP) metasurface-enhanced infrared reflection spectroscopy, or DEP-MEIRS. The DEP-MEIRS approach integrates electric, optical, and fluidic experimental techniques on a single biosensing platform. Specifically, microfluidics (for delivering live cells in aqueous medium), DEP (for attracting the cells to a metasurface-based internal reflection element), and MEIRS (for acquiring vibrational fingerprints of the cytoskeleton of the attracted cells) were combined to rapidly conduct biochemical characterization of cells in a flow. To our knowledge this is the first demonstration of the integration of a plasmonic mid-IR optical sensor with a DEP electrode. Such integration enables us to carry out rapid, continuous flow spectroscopic characterization of live cells on the time scale of minutes. The technique is equally applicable to adherent and non-adherent cells because no long-term binding of the cells to a biosensor is required – the cells attach to the metasurface *via* the DEP force that can be turned on and off as needed. The DEP forces provide the means to controllably deliver cells onto the biosensor for increased throughput and usability.

While present experiments provide modest throughput rates (of order a microliter per minute), such fluid processing speed is still higher than what can be accomplished using cell attachment to the sensor surface. Moreover, one can easily envision a variety of ways for increasing the throughput. Those include the usage of multiple microchannels and faster spectral speeds that can be accomplished using bright tunable sources of mid-infrared radiation (*e.g.*, tunable laser sources).

In addition, the layout of the DEP-MEIRS biosensor enables simultaneous acquisition of visual and spectroscopic data as shown in Fig. 5. Imaging is enabled by the semi-transparent nature of the metasurface owing to the sparse layout of metallic antennas on a transparent $CaF_2$ substrate.

Moreover, the rounded nature of the suspended cells moving with the flow facilitates conventional bright-field microscopy of the cells without necessitating any staining. The cells retain their rounded nature even after the cells are attracted to, and pushed against, the metasurface. Therefore, they are much easier to image than flat adherent cells[94] that are commonly used for spectral cytopathology,[32–34] and are generally imaged using phase-contrast microscopy. Fusion of microscopic images and spectroscopic data can potentially improve the interpretation of experimental results. By correlating the magnitude of the time-dependent vibrational fingerprints (see Fig. 5a), as well as that of the Fano resonance (see Fig. 6a) with time-dependent cell coverage (see Fig. 5c–e), we have validated the combined DEP-MEIRS technique by demonstrating that the infrared signal originates from the captured cells. This validation was facilitated by the transparency of the metasurface to visible light, which enabled us to image the cells as they were attracted to the metasurface.

The key advantage of MEIRS over transmission-based spectroscopies is its ability to probe a much smaller portion of the cellular material – mostly in the vicinity of the cell membrane – owing to the small spatial penetration depth ($l_{pen} < 100$ nm)[24] of the enhanced near-field intensity of the IR electric field.[45–47] For example, the molecular composition of a cellular membrane and cytoskeleton can undergo significant changes throughout the course of carcinogenesis, as well as under the influence of anticancer drugs.[58,95–98] An added benefit is the possibility of carrying out measurements with live cells in their natural aqueous environment because: (a) the signal is collected in reflection mode through the substrate, *i.e.* without the need to pass IR light through water, and (b) the penetration depth $l_{pen} < 100$ nm of the evanescent fields of the metasurface is considerably smaller than the thickness of a cell. Working with live cells avoids deleterious effects of fixation on the molecular composition of cells.[99,100] Avoiding fixation/drying also opens new applications avenues.

We envision a number of applications for a DEP-MEIRS sensor. As the DEP force can be repulsive as well as attractive due to the disparate dielectric properties of different cell types (*e.g.* solid tumor and blood cells),[86] it may be possible to capture one cell type (*e.g.*, epithelial cells) while preventing the other cell type (*e.g.*, blood cells) from reaching the sensor surface. The most obvious application is enumeration and phenotyping of CTCs in mixture with blood cells. By judicious choice of the AC frequency, it may be possible to exert negative (repulsive) DEP force on blood cells while exerting positive (attractive) DEP on CTCs.[70] Biochemical differences between cells (*e.g.*, between different types of CTCs) frequently manifest themselves in cytoskeleton modifications that are particularly amenable to MEIRS because of the shallow penetration depth of the evanescent metasurface-enhanced fields into the cell. For example, tumor cells with high metastatic potential,[101] as well as drug-resistant,[102] necrotic,[103] and inflammation-modified[104] cells

are known to have modified stiffness. Such changes of mechanical properties of cells have been linked to changes in their cytoskeleton[105] that could be potentially targeted by DEP-MEIRS. Spectroscopic investigation of drug effects[83] on suspension cells is another potential application of DEP-MEIRS.

An important consideration for using DEP cell capture is that it works only for a limited time because the DEP force relies in the difference in conductivities between the DEP buffer and the cytoplasm. Because the cells must be suspended in DEP buffer with much lower conductivity than their cytoplasm, the ion concentration and hence the conductivity inside the cell drops over time,[70] thereby weakening the DEP force due to the loss of conductivity contrast between the inside and outside of the cell. Cell physiology is also affected by this process. The timeframe during which significant changes of intracellular ion concentration takes place is around 30 minutes.[86] Therefore, the time between suspending the cells in DEP solution and the conclusion of the experiments was kept to a minimum, not exceeding 20 minutes. Nevertheless, more sophisticated continuous flow experimental arrangements involving continuous deionization of a flowing cell suspension[106] could enable much longer measurements. Those are needed, for example, for processing large volumes of cell solution or for investigating long-term effects of drugs on non-adherent cells.

## Experimental

### Device fabrication

Plasmonic metasurfaces with wires for external electrical connection were fabricated using electron beam (e-beam) lithography methods. E-beam resist PMMA 495k A4 was spin coated onto IR transparent $CaF_2$ substrates ($12.5 \times 12.5$ mm$^2$), exposed with e-beam on JEOL JBX9500FSZ and development in MIBK : IPA ($1:3$) solution for 90 s. 70 nm of Au was evaporated onto the samples with 10 nm Cr adhesion layer, followed by lift-off process (submerged in room temperature acetone for 16 hours). Large gold contacts were evaporated onto the edges of the samples, which are connected through bus wires with electrode wires in each metasurface pixel. 30 AWG wires were attached to the contact pads with electrically conductive adhesive (ETC Bond 556, Electron Microscopy Sciences).

There are 12 metasurface pixels on the substrate for redundancy, to protect against sporadic fabrication errors and increase the area where cells can be captured. The pixel located on the 4th position downstream the microchannel was used for measurements of cell spectra in this work. Each pixel's dimensions are $w_{pix} = 500$ μm (across the flow) and $l_{pix} = 120$ μm (along the flow), and the pixels are separated from each other by $l_{sep} = 40$ μm. Two interdigitated wires separated by $\Delta_x = 40$ μm are embedded into each of the pixels and connected to the AC voltage source. Total length of the sensing area is $l_{el} \approx 2$ mm. The dimensions are visually defined on Fig. S5.†

Microfluidic channels (length $l = 8$ mm, width $w = 0.5$mm, height $h = 64$ μm) were fabricated using standard polydimethyl siloxane (PDMS) soft lithography process. Master molds were made by cut polyimide film on flat polystyrene surface. The thickness of polyimide layer was determined using profilometer (KLA-Tencor P10). Polyimide masters were used due to facile fabrication of suitable thickness microchannel molds. PDMS (Sylgard 184, Dow) was mixed in $5:1$ base to cross-linker ratio, poured onto the mold, degassed in vacuum to remove air bubbles and heat treated in 65 °C oven for 16 hours. PDMS block was cut into shape to fit onto the $CaF_2$ piece holding the metasurfaces. Inlet and outlet ports for tubing were created in the PDMS block with a hole puncher.

Polyethylene tubing (PE-20, Instech) was inserted into the inlet and outlet ports in PDMS. Metasurface pixels on $CaF_2$ substrate were aligned with the microchannel and the two parts were clamped together using two acrylic slides. The two clamping slides (measuring 25 mm × 75 mm) were cut from 3 mm thick acrylic using laser cutter (VLS3.50, Universal Laser Systems). The top slide touching $CaF_2$ has a window to allow IR light to be transmitted to the sample unobstructed, while the bottom slide touching PDMS block has through holes for the tubing. The two acrylic slides were tightened together with bolted joints. Care was taken to apply minimal amount of pressure while tightening the joints. It is necessary that the PDMS and $CaF_2$ pieces would not separate while fluid is pumped into the microchannel, but excessive pressure could damage $CaF_2$ substrate.

### Cells solution preparation

A431 cells (human epidermoid carcinoma, ATCC CRL-1555) were cultured in Dulbecco's modified eagle medium (DMEM, Life Technologies, cat. no. 10566016) and HCT 116 cells (human colon carcinoma, ATCC CCL-247) in McCoy's 5A (modified) medium (Life Technologies, cat. no. 16600082) cell culture medium supplemented with 10% fetal bovine serum (FBS, Corning, cat. no. 35-010-CV) and 1% penicillin–streptomycin (PS, Life Technologies, cat. no. 15140122) at 37 °C and 5% $CO_2$. Cells were harvested for experiments at approximately 80% confluence. Trypsin–EDTA (0.25%, Life Technologies, cat. no. 25200056) was used to detach the cells from culture flask, followed by centrifugation at 1200 rpm for 2 minutes to pellet the cells. After centrifugation supernatant was discarded and cells were resuspended in 2 mL of fresh culture medium.

Cells were suspended in a special buffer solution (DEP solution) prior to all experiments. The DEP solution consists of ultrapure water (resistivity >18 MΩ cm) with 280 mM of sucrose (Fisher Chemical) with $1:20$ phosphate-buffered saline (PBS pH 7.2, Life Technologies) added. The conductivity of DEP solution was adjusted to $\sigma_s = 781.3 \pm 1.1$ μS cm$^{-1}$ in all experiments (measured with Oakton CON 2700 conductivity meter).

For conducting experiments, the cell suspension in culture medium was centrifuged at 2000 rpm for 2 minutes to pellet the cells. Supernatant was discarded and 2 mL of DEP solution was added, and the solution was centrifuged again. Finally, the supernatant was discarded and 1 mL of DEP solution was added. Cell concentration in the experiments was approximately $10^6$ cells per mL. The final cell solution was transferred into a 500 μL glass syringe (Model 1750 TLLX, Hamilton) and experiments were carried out immediately. The total time cells spent in the DEP solution, from the initial suspension to end of experiment, was kept under 20 minutes in each experiment.

### Cells DEP capturing and spectroscopic data acquisition

The fully assembled DEP-MEIRS microfluidic device was used in the experiments to capture cells and simultaneously measure their spectra. The metasurface on $CaF_2$ was facing microchannel side and was exposed to the cell solution pumped through the PDMS channel (as shown on Fig. 1b and c), while IR spectra of a single metasurface pixel were collected in reflection mode through the substrate. Each metasurface pixel has two long electrode wires running through it. These wires are connected to two buses, each adjacent wire connected to a different bus. The bus wires run to contact pads at the corners of $CaF_2$ substrate. Cables from function generator were connected to wires attached to the contact pads, transmitting sinusoidal AC signal to the electrodes within the metasurface, creating non-uniform electric fields in the microchannel for cell capturing.

Syringe pump (neMESYS 290N, Cetoni) was used to inject the cells in aqueous DEP solution into the microchannel at a constant flow rate ($Q = 0.01$ μL s$^{-1}$), corresponding to the Poiseuille flow with the peak speed of $v_c \approx 500$ μm s$^{-1}$ at the center of the channel. The channel was primed with DEP solution prior to cell injection. Sinusoidal AC signal was applied on the electrodes within metasurface using a function generator (33522B, Keysight Technologies). Each electrode was connected to its own signal channel, and the voltages on each channel were π out of phase. For the cells experiments, the AC voltage and frequency applied between the two wires was $V_{pp} = 14$ V (peak-to-peak) and $f^{(cell)} = 400$ kHz, respectively. Experiments were carried out at normal lab conditions ($T = 20$ °C). Heating effects due to Joule heating are not significant, as a low-conductance DEP solution was used. Heating due to dielectric loss is also not significant for the used AC signal frequency and voltage.[107] Additionally, continuous fluid flow in the microfluidic channel provides active cooling and temperature control, as the fluid is constantly being replaced by new room-temperature solution.

For spectral data acquisition, the device assembly was fitted under a Bruker Hyperion 3000 IR microscope. The microscope was equipped with 15× Cassegrain objective (NA = 0.4) and mid-IR reflection spectra were collected with liquid nitrogen cooled MCT detector. The IR microscope was coupled to Bruker Vertex 70 spectrometer fitted with KBr beamsplitter. The spectrometer, microscope and sample stage enclosure were constantly purged with dry air. Data was collected in the range of 600–7000 cm$^{-1}$ at 16 cm$^{-1}$ spectral resolution. 128 averages were taken for background measurements on gold mirror and 32 averages for collecting cell spectra. The measurement area illuminated by IR beam was 200 μm × 100 μm, defined by knife-edge aperture. The cell spectra were continuously measured and averaged after every 3 s (32 averages). Video of the sample area was recorded for collecting visual images and correlating with spectral data. Individual keyframes were extracted from the video and areas with cells were masked out to calculate the metasurface area covered with cells.

### Analysis of the cells' vibrational spectra

Temporally separated absorbance spectra were calculated from the measured cell covered metasurface reflection spectra. Reflection spectrum measured right before the cells entered the microchannel was used as the reference ($R_0$) and absorbance was calculated for each following reflection spectrum ($R_i$) using the following formula:

$$A_i = -\log(R_i/R_0), \tag{1}$$

where $A_i$ is absorbance at $i$-th time instance. All raw reflection spectra ($R_i$ and $R_0$) were normalized to the maximum peak of each spectrum (dipole peak of the metasurface resonance) prior to calculating absorbance spectra, in order to account for sporadic measurement errors.

The regions of absorbance spectra containing amide I and amide II vibrational lines (1500–1720 cm$^{-1}$) and Fano resonance peak (1250–1400 cm$^{-1}$) were used to evaluate the accumulation of cells on the sensing surface. These spectral regions were separated from the rest of the data and baseline corrected by subtracting a linear baseline (see Fig. S10†). Total area under the emerging spectral features was calculated for these baseline corrected absorbance spectra sections at each time point. Trapezoidal numerical integration was used to calculate the areas.

### Control measurements (no cells in solution)

Control measurements were carried out using 1 mL of DEP solution mixed with 1 μL of McCoy's 5A culture medium. The reason for the control measurement was to ensure that no residual cell culture medium significantly contributes to the collected IR spectra, which is attributed to the cells that are attracted onto the metasurface from the flowing cell solution. All other conditions (including the flow rate and the AC signal peak-to-peak voltage $V_{pp}$ and frequency) were identical to the experiments with cells described above. Absorbance spectra for control measurements and resulting areas under amide I, II and Fano features for each time point were calculated as above (Fig. S9†). The increase in spectral feature area over time was fitted with a linear equation (red line in Fig. S9†). The obtained slope was subtracted from the time-

varying spectral feature areas to obtain Fig. 5b and f and 6b and c.

## Microspheres solution preparation

Fluorescent polystyrene microspheres with 10 μm diameter (ThermoFisher FluoSpheres F8836, $d$ = 9.9 ± 0.1 μm, $\rho$ = 1.06 g cm$^{-3}$) were used to experimentally observe the particle capturing performance of the assembled device and compare it with simulation results. 0.5 mL of sphere solution was transferred to a conical tube and diluted with 1.5 mL of ultrapure water (resistivity >18 MΩ cm). The solution was centrifuged at 2000 rpm for 3 minutes. After centrifugation the supernatant was discarded and the sphere pellet was resuspended in 2 mL of water and centrifuged again. This process was repeated twice. After the final centrifugation and removal of supernatant, spheres were resuspended in 1 mL of water. The final sphere solution was transferred into a 500 μL glass syringe.

## DEP capture demonstration experiments for cells and microspheres

In the proof-of-principle DEP capturing experiments, the microfluidic assembly was mounted onto an Olympus IX73 inverted microscope with 10× objective. Videos of the microspheres and cells attracted to the wire electrode array were recorded with a Panasonic DMC-GH4 camera. Cells were imaged in phase contrast mode. Fluorescent microspheres were illuminated with 395 nm excitation light. The flow rate of $Q$ = 0.01 μL s$^{-1}$ was used. The sinusoidal AC voltage applied between the two wires was $V_{pp}$ = 14 V (peak-to-peak). The AC frequency was $f^{(cell)}$ = 400 kHz for the cells and $f^{(ms)}$ = 200 Hz for the microspheres. These frequencies were chosen to produce strong attracting DEP force.

In these experiments only wire electrodes were present on the CaF$_2$ sample, as the plasmonic metasurface plays less significant role in facilitating electric field generation and hence does not significantly affect the DEP force. It was advantageous to have only wire electrodes for imaging clarity. All other experimental conditions were the same as described above.

Experimental particle density as a function of distance was calculated in the $x$-direction (flow direction) from the recorded fluorescence image. The image light intensity was binarized and the fluorescence intensity values were summed at each $x$-position over the $y$-direction for the whole width of the channel. Particle density for the simulations was calculated by extracting $x$-positions of each captured particle in the simulations, assigning every particle circular shape with 10 μm diameter and calculating the equivalent $x$-distance dependent fluorescent intensity sums as for the experimental data. The density values for both cases were normalized to the highest density at the first electrode location to yield curves shown on Fig. 3d and e.

## Mathematical description of the DEP force

Dielectrophoretic forces experienced by cells in low-conductivity media with the complex-valued frequency-dependent permittivity $\tilde{\varepsilon}_s = \varepsilon + i\sigma_s/\omega$ (where the real-valued conductivity and dielectric permittivity are $\sigma_s$ and $\varepsilon_s$, respectively) have been extensively studied in the past.[69–72] To summarize, a spatially non-uniform electric field $\vec{E} = \mathrm{Re}(\vec{E}_{\backslash 0}(\vec{x})\mathrm{e}^{-i\omega t})$ with angular frequency $\omega = 2\pi f$ interacting with a live cell, presumed to be a sphere of the radius $R_{cell}$ and electric polarizability $\alpha_{cell} = 4\pi R_{cell}^3 \varepsilon_s K(f)$, exerts a DEP force given by

$$\vec{F}_{DEP} = 2\pi R_{cell}^3 \varepsilon_s K_{re}(f)\vec{\nabla}|\vec{E}_0|^2 \tag{2}$$

where $K_{cell}(f) \equiv K_{re} + iK_{im}$ is the Clausius–Mossotti (CM) factor given by eqn (3), where is also shown that $K_{re}$ is positive for high frequencies. Specifically, the DEP force attracts the cells towards the electrodes for the frequencies that are higher than the cell-dependent crossover frequency $f = f_0$.

Live cells in solution can be modeled as core–shell spherical particles with a conductive core (the cytoplasm) and insulating shell (the cellular membrane). Because of their finite polarizability (proportional to their volume), non-uniform electric fields exert a DEP force on the cells. The electric fields are AC – in the 10 kHz $< f <$ 1 MHz range – because DC electric fields do not penetrate deep into a solution due to strong Debye screening by charged ions. DEP force acting on a cell can be simplified by modeling it as a spherical core–shell particle with a highly conductive core representing a cytoplasm and a dielectric (non-conducting) shell of thickness $t_m$, radius $R_{cell}$, and dielectric permittivity $\varepsilon_m$ representing a cellular membrane. The cell is assumed to be suspended in a low-conductance fluid medium with a finite conductance $\sigma_s$, and its cytoplasm is modelled as a highly-conductive ($\sigma_{cyt} \gg \sigma_s$) core with the radius $R_{cyt} = R_{cell} - t_m \approx R_{cell}$. Under this simplified model, the cell's electric dipole moment $\vec{p}$ induced under the influence of a non-uniform quasi-static electric field $\vec{E} = \mathrm{Re}(\vec{E}_0(\vec{x})\mathrm{e}^{-i\omega t})$ with angular frequency $\omega = 2\pi f$ is given by $\vec{p} = \alpha_{cell}\vec{E}$. Note that the complex-valued frequency-dependent polarizability $\alpha_{cell}(f)$ contains both the amplitude and phase relations between the induced electric dipole moment and the electric field. Under the above simplified assumptions ($\sigma_{cyt} \gg \sigma_s$, $\sigma_s \gg \omega\varepsilon_m$, and $t_m \ll R_{cell}$), $\alpha_{cell}$ can be expressed as $\alpha_{cell} = 4\pi R_{cell}^3 \varepsilon_s K(f)$, where $K_{cell} = K_{re} + iK_{im}$ is the Clausius–Mossotti (CM) factor given by:

$$K_{cell} = \frac{1 - 2\chi^2}{1 + 4\chi^2} - i\frac{3\chi}{1 + 4\chi^2}, \tag{3}$$

where $\chi = (\sigma_s/\omega\varepsilon_m)(t_m/R_{cell})$ is a dimensionless coefficient determined by the parameters of the cellular membrane ($t_m$, $\varepsilon_m$), the overall size of the cell ($R_{cell}$), and the conductivity $\sigma_s$ of the surrounding fluid. The crossover frequency $f_0 = (\sigma_s/\sqrt{2}\pi\varepsilon_m)(t_m/R_{cell})$ corresponding to $K_{re}(f_0) = 0$ (or, equivalently, $\chi = 1/\sqrt{2}$) is determined by the geometry of the cell through the effective thickness $t_m$ of the membrane which depends on the membrane folding.[86] Eqn (3) is only valid within this highly simplified core–shell model. Therefore, $K_{re}(f)$

must be experimentally measured for every cell type, as explained in ESI† Methods ("Characterization of the frequency dependence of DEP force for cells").

The significance of the crossover frequency becomes clear when the well-known force acting on a dipole in inhomogeneous electric field, $\vec{F}_{DEP} = (\vec{p}\cdot\vec{\nabla})\vec{E}$ is time-averaged to obtain the DEP force shown in eqn (2), where a non-rotating electric field is assumed $(\vec{E}_0 \times \vec{E}_0^* = 0)$.[108] Therefore, the DEP force changes its sign at $f = f_0$.

### Numerical simulations to determine particle movement in microchannels

Commercial software COMSOL Multiphysics 5.3 was used to numerically simulate the electric fields, fluid flow patterns, and particle trajectories inside the microchannel. All quantities used in simulations were chosen to represent real values achievable in actual experiments. All simulations were run in 2D configuration, representing the center region of the microfluidic channel. A schematic of the microchannel geometry used in the simulations is shown on Fig. 3a. The electrode-forming wires (12 pairs in accordance with the experimentally realized samples) are oriented orthogonally to the flow direction along the top surface of the channel. No metasurfaces are included in the simulation because the wires primarily determine the electric fields necessary for generating the DEP force.

The simulation domain was assumed to be two-dimensional (the $x$–$y$ plane shown in Fig. 3a located at the center of the channel) because the channel width ($w_{ch}$ = 500 μm) and the length of the wire electrodes in $z$-direction are much larger than its height ($h$ = 64 μm). The flow profile (color plot on the front side of the channel on Fig. 3a) is assumed to have a parabolic velocity profile in in the $y$-direction corresponding to the Poiseuille flow. Channel height $h$ in the simulations was matched with the height of the microchannels used in experiments, fabricated using polyimide film master molds. The channel's length (along the $x$-directed flow) was $l$ = 3 mm. Fluid flow field profile was also numerically simulated to provide accurate fluid velocity values for particle trajectory calculations. Parabolic velocity profile $v_x(y)$ was used at the inlet boundary. All particles were assumed to be initially moving with the speed of the flow at their initial transverse position $y_j(t = 0)$, where $j$ is the particle label. The maximum flow velocity $v_{max}$ = 526 μm s$^{-1}$ at the center of the channel corresponding to the volumetric flow rate of $Q$ = 0.01 μ s$^{-1}$ was used in all simulations.

In the simulation, adjacent electrodes in each of the 12 pairs were assumed to have opposite polarity voltages ($+V_{pp}/2$ and $-V_{pp}/2$) corresponding to sinusoidal AC signal with peak-to-peak amplitude $V_{pp}$ = 14 V. The width and height of the wire electrodes were chosen to be $w_{el}$ = 500 nm and $h_{el}$ = 100 nm, respectively. The 12 pairs of wire electrodes were spaced out along the flow direction to accurately reproduce the fabricated sample. The wire electrode pairs separated by $\Delta_x$ = 40 μm were arranged as an array with a period of $P_x$ = 160

μm along the flow direction. Electric fields inside the channel were calculated under electrostatic assumption. Cells' radius and CM factor were assumed to be $R_{cell}$ = 10 μm and $K_{re}$ = 0.8, respectively.

Idealized center-of-mass particles with 10 μm diameter were used for particle trajectory simulations. This is equivalent to the model fluorescent polystyrene microsphere particles used in later experiments verifying simulation results (see below). Drag force, DEP force, and gravitational force were acting on the particles. Forces were calculated using results from previous fluid velocity field and electric field simulations. The equation of motion solved for particles was:

$$\frac{d(m_p\vec{v})}{dt} = \vec{F}_D + \vec{F}_{DEP} + \vec{F}_g, \tag{4}$$

where $m_p$ is the mass of particle, $\vec{v}$ is the velocity of particle and $\vec{F}_D$, $\vec{F}_{DEP}$ and $\vec{F}_g$ are drag, DEP, and gravitational forces, respectively. Drag force had the form:

$$\vec{F}_D = \frac{9}{2}\frac{\mu m_p}{\rho_p R_p^2}(\vec{u} - \vec{v}), \tag{5}$$

where $\mu$ is dynamic viscosity of the fluid (water), $\rho_p$ is the density of the particle (here $\rho_p$ = 1.06 g cm$^{-3}$), $R_p$ is the radius of the particle, and $\vec{u}$ is the fluid velocity (found previously). DEP force was calculated using eqn (2) (electric field found previously). Gravitational force had the form:

$$\vec{F}_g = m_p\vec{g}\frac{\rho_p - \rho}{\rho_p}, \tag{6}$$

where $\rho$ is the density of the fluid (water) and $\vec{g}$ is a vector with magnitude equal to the standard gravity ($g_0$) and direction towards $y$.

1000 particles were injected with the density of particles in the direction perpendicular to flow ($y$-direction) being proportional to the fluid velocity at the inlet (i.e. more particles at the center of the channel where fluid velocity is higher). Particle trajectory calculations were terminated at $\delta y_{min}$ = 5 μm from the channel top and bottom surfaces, corresponding to the radius of the particles in the simulation. Freeze condition was applied at the domain walls, i.e. particles stopped at the point where they touch the bounding surfaces.

## Conflicts of interest

There are no conflicts to declare.

## Acknowledgements

# References

1 W. W. Johnston, The malignant pleural effusion. A review of cytopathologic diagnoses of 584 specimens from 472 consecutive patients, *Cancer*, 1985, **56**(4), 905.

2 C. Ravetto, L. Colombo and M. E. Dottorini, Usefulness of fine-needle aspiration in the diagnosis of thyroid carcinoma, *Cancer Cytopathol.*, 2001, **90**(6), 357.

3 K. A. Atkins and C. N. Powers, The Cytopathology of Infectious Diseases, *Adv. Anat. Pathol.*, 2002, **9**(1), 52.

4 S. Bigner and W. Jonston, The cytopathology of cerebrospinal fluid. I. Nonneoplastic conditions, lymphoma and leukemia, *Acta Cytol.*, 1981, **25**(4), 345.

5 M. N. Gurcan, L. E. Boucheron, A. Can, A. Madabhushi, N. M. Rajpoot and B. Yener, Histopathological Image Analysis: A Review, *IEEE R. Bio-Med Eng.*, 2009, **2**, 147.

6 M. Fahey, L. Irwig and P. Macaskill, Meta-analysis of Pap test accuracy, *Am. J. Epidemiol.*, 1995, **141**, 680.

7 W. J. Frable, Fine-needle aspiration biopsy: a review, *Hum. Pathol.*, 1983, **14**(1), 9.

8 T. Davidov, S. Z. Trooskin, B.-A. Shanker, D. Yip, O. Eng, J. Crystal, J. Hu, V. S. Chernyavsky, M. F. Deen, M. May and R. L. Artymyshyn, Routine second-opinion cytopathology review of thyroid fine needle aspiration biopsies reduces diagnostic thyroidectomy, *Surgery*, 2010, **148**(6), 1294.

9 K. Gajjar, A. A. Ahmadzai, G. Valasoulis, J. Trevisan, M. Nasioutziki, A. Loufopoulos, M. Kyrgiou, S. M. Stasinou, P. Karakitsos, E. Paraskevaidis, B. Da Gama-Rose, P. L. Martin-Hirsch and F. L. Martin, Histology Verification Demonstrates That Biospectroscopy Analysis of Cervical Cytology Identifies Underlying Disease More Accurately than Conventional Screening: Removing the Confounder of Discordance, *PLoS One*, 2014, **9**(1), e82416.

10 M. H. Stoler and M. Schiffman, Interobserver reproducibility of cervical cytologic and histologic interpretations: Realistic estimates from the ascus-lsil triage study, *JAMA, J. Am. Med. Assoc.*, 2001, **285**(11), 1500.

11 G. Raghu, Y. N. Mageto, D. Lockhart, R. A. Schmidt, D. E. Wood and J. D. Godwin, The Accuracy of the Clinical Diagnosis of New-Onset Idiopathic Pulmonary Fibrosis and Other Interstitial Lung Disease: A Prospective Study, *Chest*, 1999, **116**(5), 1168.

12 K. Savage, S. Leung, S. K. Todd, L. A. Brown, R. L. Jones, D. Robertson, M. James, S. Parry, S. M. Rodrigues Pinilla, D. Huntsman and J. S. Reis-Filho, Distribution and significance of caveolin 2 expression in normal breast and invasive breast cancer: an immunofluorescence and immunohistochemical analysis, *Breast Cancer Res. Treat.*, 2008, **110**(2), 245.

13 W. Yamagami, N. Susumu, H. Tanaka, A. Hirasawa, K. Banno, N. Suzuki, H. Tsuda, K. Tsukazaki and D. Aoki, Immunofluorescence-Detected Infiltration of CD4+FOXP3+ Regulatory T Cells is Relevant to the Prognosis of Patients With Endometrial Cancer, *Int. J. Gynecol. Cancer*, 2011, **9**, 1628.

14 C. Chen, J. Peng, H.-S. Xia, G.-F. Yang, Q.-S. Wu, L.-D. Chen, L.-B. Zeng, Z.-L. Zhang, D.-W. Pang and Y. Li, Quantum dots-based immunofluorescence technology for the quantitative determination of HER2 expression in breast cancer, *Biomaterials*, 2009, **30**(15), 2912.

15 C.-H. Wu, Y.-Y. Huang, P. Chen, K. Hoshino, H. Liu, E. P. Frenkel, J. X. J. Zhang and K. V. Sokolov, Versatile Immunomagnetic Nanocarrier Platform for Capturing Cancer Cells, *ACS Nano*, 2013, **7**(10), 8816.

16 Y.-Y. Huang, K. Hoshino, P. Chen, C.-H. Wu, N. Lane, M. Huebschman, H. Liu, K. Sokolov, J. W. Uhr, E. P. Frenkel and J. X. Zhang, Immunomagnetic nanoscreening of circulating tumor cells with a motion controlled microfluidic system, *Biomed. Microdevices*, 2013, **15**(4), 673.

17 G. Spizzo, D. Fong, M. Wurm, C. Ensinger, P. Obrist, C. Hofer, G. Mazzoleni, G. Gastl and P. Went, EpCAM expression in primary tumour tissues and metastases: an immunohistochemical analysis, *J. Clin. Pathol.*, 2011, **64**(5), 415.

18 S. Riethdorf, H. Fritsche, V. Müller, T. Rau, C. Schindlbeck, B. Rack, W. Janni, C. Coith, K. Beck, F. Jänicke, S. Jackson, T. Gornet, M. Cristofanilli and K. Pantel, Detection of Circulating Tumor Cells in Peripheral Blood of Patients with Metastatic Breast Cancer: A Validation Study of the CellSearch System, *Clin. Cancer Res.*, 2007, **13**(3), 920.

19 K. Pantel and C. Alix-Panabières, Real-time Liquid Biopsy in Cancer Patients: Fact or Fiction?, *Cancer Res.*, 2013, **73**(21), 6384.

20 S. Martin, H.-Z. Zhang, E. Magyarosy, E. Jaffe, S.-M. Hsu and E. Chu, Immunologic Methods in Cytology: Definitive Diagnosis of Non-Hodgkin's Lymphomas Using Immunologic Markers for T- and B-Cells, *Am. J. Clin. Pathol.*, 1984, **82**, 666.

21 D. Char, B.-M. Ljung, J. Deschenes and T. Miller, Intraocular lymphoma: immunological and cytological analysis, *Br. J. Ophthalmol.*, 1988, **72**, 905.

22 M. J. Adams, *Chemometrics in Analytical Spectroscopy*, Royal Society of Chemistry, Cambridge, U.K., 2nd edn, 2004.

23 K. Papamarkakis, B. Bird, J. M. Schubert, M. Miljković, R. Wein, K. Bedrossian, N. Laver and M. Diem, Cytopathology by optical methods: spectral cytopathology of the oral mucosa, *Lab. Invest.*, 2010, **90**, 589.

24 G. Kelp, N. Arju, A. Lee, E. Esquivel, R. Delgado, Y. Yu, S. Dutta-Gupta, K. Sokolov and G. Shvets, Application of metasurface-enhanced infra-red spectroscopy to distinguish between normal and cancerous cell types, *Analyst*, 2019, **144**(4), 1115–1127.

25 G. Bellisola and C. Sorio, Infrared spectroscopy and microscopy in cancer research and diagnosis, *Am. J. Cancer Res.*, 2012, **2**(1), 1.

26 M. Diem, M. Miljković, B. Bird, T. Chernenko, J. Schubert, E. Marcsisin, A. Mazur, E. Kingston, E. Zuser, K. Papamarkakis and N. Laver, Applications of Infrared and Raman Microspectroscopy of Cells and Tissue in Medical Diagnostics: Present Status and Future Promises, *Spectroscopy*, 2012, **27**, 848360.

27 M. Miljković, B. Bird, K. Lenau, A. I. Mazur and M. Diem, Spectral cytopathology: new aspects of data collection,

manipulation and confounding effects, *Analyst*, 2013, **138**(14), 3975.

28 S. Kulka, N. Kaun, J. R. Baena, J. Frank, P. Svasek, D. Moss, M. J. Vellekoop and B. Lendl, Mid-IR synchrotron radiation for molecular specific detection in microchip-based analysis systems, *Anal. Bioanal. Chem.*, 2004, **378**(7), 1735.

29 L. Vaccari, G. Birarda, L. Businaro, S. Pacor and G. Grenci, Infrared Microspectroscopy of Live Cells in Microfluidic Devices (MD-IRMS): Toward a Powerful Label-Free Cell-Based Assay, *Anal. Chem.*, 2012, **84**(11), 4768.

30 E. Mitri, G. Birarda, L. Vaccari, S. Kenig, M. Tormen and G. Grenci, SU-8 bonding protocol for the fabrication of microfluidic devices dedicated to FTIR microspectroscopy of live cells, *Lab Chip*, 2014, **14**(1), 210.

31 H.-Y. N. Holman, R. Miles, Z. Hao, E. Wozei, L. M. Anderson and H. Yang, Real-Time Chemical Imaging of Bacterial Activity in Biofilms Using Open-Channel Microfluidics and Synchrotron FTIR Spectromicroscopy, *Anal. Chem.*, 2009, **81**(20), 8564.

32 J. Tittus, C. Flfili, J. K. Hilliard, J. A. Ward and A. G. U. Perera, Early detection of cell activation events by means of attenuated total reflection Fourier transform infrared spectroscopy, *Appl. Phys. Lett.*, 2014, **104**, 243705.

33 M. Hermes, R. Brandstrup Morrish, L. Huot, L. Meng, S. Junaid, J. Tomko, G. R. Lloyd, W. T. Masselink, P. Tidemand-Lichtenberg and C. Pedersen, Mid-IR hyperspectral imaging for label-free histopathology and cytology, *J. Opt.*, 2018, **20**(2), 023002.

34 S. Kazarian and K. Chan, Applications of ATR-FTIR spectroscopic imaging to biomedical samples, *Biochim. Biophys. Acta, Biomembr.*, 2006, **1758**(7), 858.

35 D. I. Ellis, D. P. Cowcher, L. Ashton, S. O'Hagan and R. Goodacre, Illuminating disease and enlightening biomedicine: Raman spectroscopy as a diagnostic tool, *Analyst*, 2013, **138**(14), 3871.

36 A. B. Veloso, J. P. F. Longo, L. A. Muehlmann, B. F. Tollstadius, P. E. N. Souza, R. B. Azevedo, P. C. Morais and S. W. da Silva, SERS Investigation of Cancer Cells Treated with PDT: Quantification of Cell Survival and Follow-up, *Sci. Rep.*, 2017, **7**(1), 7175.

37 E. C. Faria and P. Gardner, Single-Cell Analysis, in *Methods Mol. Biol.*, Humana Press, 2012, p. 151.

38 H. Byrne, G. Sockalingum and N. Stone, *Biomedical Applications of Synchrotron Infrared Microspectroscopy*, The Royal Society of Chemistry, 2011.

39 W. E. Huang, L. Mengqui, R. M. Jarvis and R. Goodacre, Shining Light on the Microbial World: The Application of Raman Microspectroscopy, *Adv. Appl. Microbiol.*, 2010, **70**, 153.

40 J. W. Chan and D. K. Lieu, Label-free biochemical characterization of stem cells using vibrational spectroscopy, *J. Biophotonics*, 2009, **2**(11), 656.

41 K. Ataka, S. T. Stripp and J. Heberle, Surface-enhanced infrared absorption spectroscopy (SEIRAS) to probe monolayers of membrane proteins, *Biochim. Biophys. Acta, Biomembr.*, 2013, **1828**(10), 2283.

42 G. I. Dovbeshko, V. I. Chegel, N. Y. Gridina, O. P. Repnytska, Y. M. Shirshov, V. P. Tryndiak, I. M. Todor and G. I. Solyanik, Surface enhanced IR absorption of nucleic acids from tumor cells: FTIR reflectance study, *Biopolymers*, 2002, **67**(6), 470.

43 E. Zaitseva, M. Saavedra, S. Banerjee, T. P. Sakmar and R. Vogel, SEIRA Spectroscopy on a Membrane Receptor Monolayer Using Lipoprotein Particles as Carriers, *Biophys. J.*, 2010, **99**(7), 2327.

44 D. Millo, P. Hildebrandt, M.-E. Pandelia, W. Lubitz and I. Zebger, SEIRA Spectroscopy of the Electrochemical Activation of an Immobilized [NiFe] Hydrogenase under Turnover and Non-Turnover Conditions, *Angew. Chem., Int. Ed.*, 2011, **50**(11), 2632.

45 N. Arju, T. Ma, A. Khanikaev, D. Purtseladze and G. Shvets, Optical Realization of Double-Continuum Fano Interference and Coherent Control in Plasmonic Metasurfaces, *Phys. Rev. Lett.*, 2015, **114**(23), 237403.

46 S. Aksu, A. A. Yanik, R. Adato, A. Artar, M. Huang and H. Altug, High-Throughput Nanofabrication of Infrared Plasmonic Nanoantenna Arrays for Vibrational Nanospectroscopy, *Nano Lett.*, 2010, **10**(7), 2511.

47 C. Wu, A. B. Khanikaev, R. Adato, N. Arju, A. A. Yanik, H. Altug and G. Shvets, Fano-resonant asymmetric metamaterials for ultrasensitive spectroscopy and identification of molecular monolayers, *Nat. Mater.*, 2012, **11**, 69.

48 R. Adato and H. Altug, In-situ ultra-sensitive infrared absorption spectroscopy of biomolecule interactions in real time with plasmonic nanoantennas, *Nat. Commun.*, 2013, **4**, 2154.

49 R. Adato, A. A. Yanik, J. J. Amsden, D. L. Kaplan, F. G. Omenetto, M. K. Hong, S. Erramilli and H. Altug, Ultra-sensitive vibrational spectroscopy of protein monolayers with plasmonic nanoantenna arrays, *Proc. Natl. Acad. Sci. U. S. A.*, 2009, **106**(46), 19227.

50 D. Etezadi, J. B. Warner, H. A. Lashuel and H. Altug, Real-Time In Situ Secondary Structure Analysis of Protein Monolayer with Mid-Infrared Plasmonic Nanoantennas, *ACS Sens.*, 2018, **3**(6), 1109.

51 M. J. Baker, J. Trevisan, P. Bassan, R. Bhargava, H. J. Butler, K. M. Dorling, P. R. Fielden, S. W. Fogarty, N. J. Fullwood, K. A. Heys, C. Hughes, P. Lasch, P. L. Martin-Hirsch, B. Obinaju, G. D. Sockalingum, J. Sulé-Suso, R. J. Strong, M. J. Walsh, B. R. Wood, P. Gardner and F. L. Martin, Using Fourier transform IR spectroscopy to analyze biological materials, *Nat. Protoc.*, 2014, **9**, 1771.

52 M. J. Walsh, M. N. Singh, H. F. Stringfellow, H. M. Pollock, A. Hammiche, O. Grude, N. J. Fullwood, M. A. Pitt, P. L. Martin-Hirsch and F. L. Martin, FTIR Microspectroscopy Coupled with Two-Class Discrimination Segregates Markers Responsible for Inter- and Intra-Category Variance in Exfoliative Cervical Cytology, *Biomarker Insights*, 2008, **3**, BMI.S592.

53 M. J. Walsh, M. J. German, M. Singh, H. M. Pollock, A. Hammiche, M. Kyrgiou, H. F. Stringfellow, E. Paraskevaidis,

P. L. Martin-Hirsch and F. L. Martin, IR microspectroscopy: potential applications in cervical cancer screening, *Cancer Lett.*, 2007, **246**(1), 1.

54 M. K. Kuimova, K. L. A. Chan and S. G. Kazarian, Chemical Imaging of Live Cancer Cells in the Natural Aqueous Environment, *Appl. Spectrosc.*, 2009, **63**(2), 164.

55 K. L. A. Chan and S. G. Kazarian, Aberration-free FTIR spectroscopic imaging of live cells in microfluidic devices, *Analyst*, 2013, **138**(14), 4040.

56 L. Vaccari, G. Birarda, G. Grenci, S. Pacor and L. Businaro, Synchrotron radiation infrared microspectroscopy of single living cells in microfluidic devices: advantages, disadvantages and future perspectives, *J. Phys.: Conf. Ser.*, 2012, **359**(1), 012007.

57 X. Cheng, Y.-S. Liu, D. Irimia, U. Demirci, L. Yang, L. Zamir, W. R. Rodríguez, M. Toner and R. Bashir, Cell detection and counting through cell lysate impedance spectroscopy in microfluidic devices, *Lab Chip*, 2007, **7**(6), 746.

58 P. L. Fale, A. Altharawi and K. A. Chan, In situ Fourier transform infrared analysis of live cells' response to doxorubicin, *Biochim. Biophys. Acta*, 2015, **1853**, 2640.

59 K.-I. Miyamoto, P. Yamada, R.-T. Yamaguchi, T. Muto, A. Hirano, Y. Kimura, M. Niwano and H. Isoda, In situ observation of a cell adhesion and metabolism using surface infrared spectroscopy, *Cytotechnology*, 2007, **55**, 143–149.

60 H. Suzuki, Y. Yanase, T. Tsutsui, K. Ishii, T. Hiragun and M. Hide, Applying Surface Plasmon Resonance to Monitor the IgE-Mediated Activation of Human Basophils, *Allergol. Int.*, 2008, **57**, 347.

61 A. L. Stelling, D. Toher, O. Uckermann, J. Tavkin, E. Leipnitz, J. Schweizer, H. Cramm, G. Steiner, K. D. Geiger and M. Kirsch, Infrared Spectroscopic Studies of Cells and Tissues: Triple Helix Proteins as a Potential Biomarker for Tumors, *PLoS One*, 2013, **8**(3), e58332.

62 M. Grube, K. Shvirksts, C. Krafft, S. Kokorevich, E. Zandberga, A. Abols, A. Line and U. Kalnenieks, Miniature diamond-anvil cells for FTIR-microspectroscopy biosamples, *Analyst*, 2018, **143**, 3595.

63 R. B. M. Schasfoort, F. Abali, I. Stojanovic, G. Vidarsson and L. W. M. M. Terstappen, Trends in SPR Cytometry: Advances in Label-Free Detection of Cell Parameters, *Biosensors*, 2018, **8**, 102.

64 M. J. Rosenbluth, W. A. Lam and D. A. Fletcher, Force Microscopy of Nonadherent Cells: A Comparison of Leukemia Cell Deformability, *Biophys. J.*, 2006, **90**, 2994.

65 E. Suraniti, E. Sollier, R. Calemczuk, T. Livache, P. N. Marche, M.-B. Villiers and Y. Roupioz, Real-time detection of lymphocytes binding on an antibody chip using SPR imaging, *Lab Chip*, 2007, **7**, 1206.

66 F. Cerignoli, Y. A. Abassi, B. J. Lamarche, G. Guenther, D. S. Ana, D. Guimet, W. Zhang, J. Zhang and B. Xi, In vitro immunotherapy potency assays using real-time cell analysis, *PLoS One*, 2018, **13**, e0193498.

67 A. Revzin, K. Sekine, A. Sin, R. G. Tompkins and M. Toner, Development of a microfabricated cytometry platform for

characterization and sorting of individual leukocytes, *Lab Chip*, 2005, **5**, 30.

68 H. Zhu, J. Yan and A. Revzin, Catch and release cell sorting: Electrochemical desorption of T-cells from antibody-modified microelectrodes, *Colloids Surf., B*, 2008, **64**, 260.

69 I. F. Cheng, W. L. Huang, T. Y. Chen, C. W. Liu, Y. D. Lin and W. C. Su, Antibody-free isolation of rare cancer cells from blood based on 3D lateral dielectrophoresis, *Lab Chip*, 2015, **15**(14), 2950.

70 P. R. Gascoyne, J. Noshari, T. J. Anderson and F. F. Becker, Isolation of Rare Cells from Cell Mixtures by Dielectrophoresis, *Electrophoresis*, 2009, **30**(8), 1388.

71 V. Gupta, I. Jafferji, M. Garza, V. O. Melnikova, D. K. Hasegawa, R. Pethig and D. W. Davis, ApoStream™, a new dielectrophoretic device for antibody independent isolation and recovery of viable cancer cells from blood, *Biomicrofluidics*, 2012, **6**(2), 024133.

72 C. Huang, H. Liu, N. H. Bander and B. J. Kirby, Enrichment of prostate cancer cells from blood cells with a hybrid dielectrophoresis and immunocapture microfluidic system, *Biomed. Microdevices*, 2013, **15**(6), 941.

73 I.-F. Cheng, H.-C. Chang, T.-Y. Chen, C. Hu and F.-L. Yang, Rapid (<5 min) Identification of Pathogen in Human Blood by Electrokinetic Concentration and Surface-Enhanced Raman Spectroscopy, *Sci. Rep.*, 2013, **3**, 2365.

74 I.-F. Cheng, C.-C. Lin, D.-Y. Lin and H.-C. Chang, A dielectrophoretic chip with a roughened metal surface for on-chip surface-enhanced Raman scattering analysis of bacteria, *Biomicrofluidics*, 2010, **4**(3), 034104.

75 G. Birarda, A. Ravasio, M. Suryana, S. Maniam, H.-Y. N. Holman and G. Grenci, IR-Live: fabrication of a low-cost plastic microfluidic device for infrared spectromicroscopy of living cells, *Lab Chip*, 2016, **16**(9), 1644.

76 K. L. A. Chan, X. Niu, A. J. de Mello and S. G. Kazarian, Rapid prototyping of microfluidic devices for integrating with FT-IR spectroscopic imaging, *Lab Chip*, 2010, **10**(16), 2170.

77 B. Lehmkuhl, S. D. Noblitt, A. T. Krummel and C. S. Henry, Fabrication of IR-transparent microfluidic devices by anisotropic etching of channels in CaF2, *Lab Chip*, 2015, **15**(22), 4364.

78 T. Pan, R. T. Kelly, M. C. Asplund and A. T. Woolley, Fabrication of calcium fluoride capillary electrophoresis microdevices for on-chip infrared detection, *J. Chromatogr. A*, 2004, **1027**(1), 231.

79 C. Matthäus, B. Bird, M. Miljković, T. Chernenko, M. Romeo and M. Diem, Infrared and Raman Microscopy in Cell Biology, *Methods Cell Biol.*, 2008, **89**, 275.

80 M. Jimenez-Hernandez, C. Hughes, P. Bassan, F. Ball, M. D. Brown, N. W. Clarke and P. Gardner, Exploring the spectroscopic differences of Caki-2 cells progressing through the cell cycle while proliferating in vitro, *Analyst*, 2013, **138**(14), 3957.

81 V. K. Katukuri, J. Hargrove, S. J. Miller, K. Rahal, J. Y. Kao, R. Wolters, E. M. Zimmermann and T. D. Wang, Detection of colonic inflammation with Fourier transform infrared

spectroscopy using a flexible silver halide fiber, *Phys. Med. Biol.*, 2010, **1**(3), 1014.

82  S. Y. Lee, K.-A. Yoon, S. H. Jang, E. O. Ganbold, D. Uuriintuya, S.-M. Shin, P. D. Ryu and S.-W. Joo, Infrared spectroscopy characterization of normal and lung cancer cells originated from epithelium, *J. Vet. Sci.*, 2009, **10**(4), 299.

83  A. Derenne, R. Gasper and E. Goormaghtigh, The FTIR spectrum of prostate cancer cells allows the classification of anticancer drugs according to their mode of action, *Analyst*, 2011, **136**(6), 1134.

84  K. L. Andrew Chan and S. G. Kazarian, Attenuated total reflection Fourier-transform infrared (ATR-FTIR) imaging of tissues and live cells, *Chem. Soc. Rev.*, 2016, **45**(7), 1850.

85  H.-S. Moon, K. Kwon, S.-I. Kim, H. Han, J. Sohn, S. Lee and H.-I. Jung, Continuous separation of breast cancer cells from blood samples using multi-orifice flow fractionation (MOFF) and dielectrophoresis (DEP), *Lab Chip*, 2011, **11**(6), 1118.

86  R. P. Gascoyne and S. Shim, Isolation of Circulating Tumor Cells by Dielectrophoresis, *Cancers*, 2014, **6**(1), 545.

87  S. Shim, K. Stemke-Hale, J. Noshari, F. F. Becker and P. R. C. Gascoyne, Dielectrophoresis has broad applicability to marker-free isolation of tumor cells from blood by microfluidic systems, *Biomicrofluidics*, 2013, **7**, 011808.

88  K. Khoshmanesh, C. Zhang, S. Nahavandi, F. J. Tovar-Lopez, S. Baratchi, A. Mitchell and K. Kalantar-zadeh, Size based separation of microparticles using a dielectrophoretic activated system, *J. Appl. Phys.*, 2010, **108**(3), 034904.

89  Y. Huang and R. Pethig, Electrode design for negative dielectrophoresis, *Meas. Sci. Technol.*, 1991, **2**(12), 1142.

90  Y. Huang, R. Holzel, R. Pethig and X.-B. Wang, Differences in the AC electrodynamics of viable and non-viable yeast cells determined through combined dielectrophoresis and electrorotation studies, *Phys. Med. Biol.*, 1992, **37**(7), 1499.

91  A. Nakano and A. Ros, Protein Dielectrophoresis: Advances, Challenges and Applications, *Electrophoresis*, 2013, **34**(7), 1085.

92  K.-T. Liao, M. Tsegaye, V. Chaurey, C.-F. Chou and N. S. Swami, Nano-constriction device for rapid protein preconcentration in physiological media through a balance of electrokinetic forces, *Electrophoresis*, 2012, **33**(13), 1958.

93  K.-T. Liao and C.-F. Chou, Nanoscale Molecular Traps and Dams for Ultrafast Protein Enrichment in High-Conductivity Buffers, *J. Am. Chem. Soc.*, 2012, **134**(21), 8742.

94  L. L. Drey, M. C. Graber and J. Bieschke, Counting unstained, confluent cells by modified bright-field microscopy, *BioTechniques*, 2013, **55**, 1.

95  M. A. Hollingsworth and B. J. Swanson, Mucins in cancer, *Nat. Rev. Cancer*, 2004, **4**(1), 45.

96  U. Cavallaro and G. Christofori, Cell adhesion and signalling by cadherins and Ig-CAMs in cancer, *Nat. Rev. Cancer*, 2004, **4**, 118.

97  M. P. Clausen, H. Colin-York, F. Schneider, C. Eggeling and M. Fritzsche, Dissecting the actin cortex density and membrane-cortex distance in living cells by super-resolution, *J. Phys. D: Appl. Phys.*, 2017, **50**(6), 064002.

98  J. Wang, H. Qi, X. Zhang, W. Si, F. Xu, T. Hou, H. Zhou, A. Wang, G. Li, Y. Liu, Y. Fang, H. Piao and X. Liang, Saikosaponin D from Radix Bupleuri suppresses triple-negative breast cancer cell growth by targeting β-catenin signaling, *Biomed. Pharmacother.*, 2018, **108**, 724.

99  A. I. Mazur, E. J. Marcsisin, B. Bird, M. Miljković and M. Diem, Evaluating Different Fixation Protocols for Spectral Cytopathology, Part 1, *Anal. Chem.*, 2012, **84**(3), 1259.

100  A. J. Hobro and N. I. Smith, An evaluation of fixation methods: Spatial and compositional cellular changes observed by Raman imaging, *Vib. Spectrosc.*, 2017, **91**, 31.

101  W. Xu, R. Mezencev, B. Kim, L. Wang, J. McDonald and T. Sulchek, Cell Stiffness Is a Biomarker of the Metastatic Potential of Ovarian Cancer Cells, *PLoS One*, 2012, **7**, e46609.

102  M. Islam, R. Mezencev, B. McFarland, H. Brink, B. Campbell, B. Tasadduq, E. K. Waller, W. Lam, A. Alexeev and T. Sulchek, Microfluidic cell sorting by stiffness to examine heterogenic responses of cancer cells to chemotherapy, *Cell Death Dis.*, 2018, **9**, 239.

103  H. Liu, N. Wang, Z. Zhang, H. Wang, J. Du and J. Tang, Effects of Tumor Necrosis Factor-α on Morphology and Mechanical Properties of HCT116 Human Colon Cancer Cells Investigated by Atomic Force Microscopy, *Scanning*, 2017, **2017**, 2027079.

104  N. Bufi, M. Saitakis, S. Dogniaux, O. Buschinger, A. Bohineust, A. Richert, M. Maurin, C. Hivroz and A. Asnacios, Human Primary Immune Cells Exhibit Distinct Mechanical Properties that Are Modified by Inflammation, *Biophys. J.*, 2015, **108**, 2181.

105  W. A. Lam, M. J. Rosenbluth and D. A. Fletcher, Chemotherapy exposure increases leukemia cell stiffness, *Blood*, 2007, **109**, 3505.

106  S. Shim, K. Stemke-Hale, A. M. Tsimberidou, J. Noshari, T. E. Anderson and P. R. C. Gascoyne, Antibody-independent isolation of circulating tumor cells by continuous-flow dielectrophoresis, *Biomicrofluidics*, 2013, **7**, 011807.

107  T. J. Kwak, I. Hossen, R. Bashir, W.-J. Chang and C. H. Lee, Localized Dielectric Loss Heating in Dielectrophoresis Devices, *Sci. Rep.*, 2019, **9**, 18977.

108  T. B. Jones, Basic Theory of Dielectrophoresis and Electrorotation, *IEEE Eng. Med. Biol.*, 2003, **22**(6), 33.